Delft University of Technology

A viscoplasticity model with an invariant-based non-Newtonian flow rule for unidirectional thermoplastic composites

Hofman, P.; Kovačević, D.; van der Meer, F. P.; Sluys, L. J.

Important note
To cite this publication, please use the final published version (if applicable).
Please check the document version above.

Research paper

A viscoplasticity model with an invariant-based non-Newtonian flow rule for unidirectional thermoplastic composites

P. Hofman *, D. Kovačević, F.P. van der Meer, L.J. Sluys

Delft University of Technology, Delft, Netherlands

ARTICLE INFO

ABSTRACT

A three-dimensional mesoscopic viscoplasticity model for simulating rate-dependent plasticity and creep in unidirectional thermoplastic composites is presented. The constitutive model is a transversely isotropic extension of an isotropic finite strain viscoplasticity model for neat polymers. Rate-dependent plasticity and creep are described by a non-Newtonian flow rule where the viscosity of the material depends on an equivalent stress measure through an Eyring-type relation. In the present formulation, transverse isotropy is incorporated by defining the equivalent stress measure and flow rule as functions of transversely isotropic stress invariants. In addition, the Eyring-type viscosity function is extended with anisotropic pressure dependence. As a result of the formulation, plastic flow in fiber direction is effectively excluded and pressure dependence of the polymer matrix is accounted for. The re-orientation of the transversely isotropic plane during plastic deformations is incorporated in the constitutive equations, allowing for an accurate large deformation response. The formulation is fully implicit and a consistent linearization of the algorithmic constitutive equations is performed to derive the consistent tangent modulus. The performance of the mesoscopic constitutive model is assessed through a comparison with a micromechanical model for carbon/PEEK, with the original isotropic viscoplastic version for the polymer matrix and with hyperelastic fibers. The micromodel is first used to determine the material parameters of the mesoscale model with a few stress–strain curves. It is demonstrated that the mesoscale model gives a similar response to the micromodel under various loading conditions. Finally, the mesoscale model is validated against off-axis experiments on unidirectional thermoplastic composite plies.

1. Introduction

Unidirectional fiber reinforced polymer composites are increasingly used in the aerospace and automotive industry because of their appealing properties. These materials, with superior stiffness and strength compared to more traditional metallic materials, allow for lighter structural components, resulting in significant weight-savings in airplanes and automobiles and therefore less fuel consumption and environmental impact (Timmis et al., 2015).

In recent years, there has been a growing interest in the use of thermoplastics in fiber reinforced polymer composites. Structural elements made of thermoplastic composites can be fusion bonded, without the need of additional materials such as adhesives or bolts, resulting in more weight-savings, faster processing cycles and the possibility to manufacture composite parts with more complex geometries. However, the mechanical performance of these fusion bonded thermoplastic composites strongly depends on the processing conditions (Valverde et al., 2018, 2020; Akkerman et al., 2020; Neveu et al., 2022). At present, the understanding of processing effects on the mechanical response is not fully matured and the lack of sophisticated performance prediction tools forms an obstacle to the wide-spread use of fusion bonded thermoplastic composites. To improve the prediction abilities, it is essential to develop accurate, efficient and robust constitutive models, capable of simulating the material response under short- and long-term loadings.

A constitutive model that unifies stain-rate dependent yielding and creep in glassy polymers is the Eindhoven Glassy Polymer (EGP) model (Tervoort et al., 1996, 1998; Govaert et al., 2000; Klompen et al., 2005; Van Breemen et al., 2011; Lenders et al., 2023). This is an isotropic viscoplastic model and is part of a family of models for polymers without an explicit yield function (Haward and Thackray, 1968; Boyce et al., 1988, 1992). Instead of a separation in an elastic and plastic response, it is assumed that an applied stress always produces plastic flow and that the rate of plastic flow depends on the stress level. The rate of plastic deformation is then described with a non-Newtonian flow rule following an Eyring-type relation (Eyring, 1936).

The isotropic EGP model has been successfully applied to micromechanical analyses of polymer composites with representative volume elements (Kovačević et al., 2022; Lenders et al., 2024; Kovačević et al., 2024), where fibers and matrix are explicitly modeled. A representative volume element is sufficient for studying the composites' behavior under homogeneous deformations at the mesoscale level—that is, the level at which the composite can be considered a homogeneous medium. For more complex structural analyses of composites with inhomogeneous deformations, a multiscale approach can be used. This requires a coupling between the microscale and mesoscale, where two finite element analyses are performed simultaneously and information is exchanged in between. However, such approaches remain computationally infeasible and are still subject of ongoing research in the case of localization (Oliver et al., 2015; Ke and Van Der Meer, 2022). To overcome the computational burden of multiscale analyses, either surrogate models (Maia et al., 2023, 2025), homogenized micromechanics-based models (Larsson et al., 2020; Singh et al., 2023) or mesoscopic phenomenological constitutive models are required.

Extensions of the EGP model for simulating anisotropic rate-dependent plasticity and creep have previously been proposed (Van Erp et al., 2009; Senden et al., 2013; Amiri-Rad et al., 2019; Amiri-Rad et al., 2021). The key element in these works is the incorporation of anisotropy in the (hyper-)elasticity and rate-dependent plasticity relations. Van Erp et al. (2009) proposed an anisotropic flow rule based on the classical Hill yield criterion (Hill, 1948). Senden et al. (2013) used this flow rule in the EGP model for predicting anisotropic yielding in injection molded polyethylene and Amiri-Rad et al. further developed it for *short* fiber (Amiri-Rad et al., 2019) and *long* fiber reinforced polymer composites (Amiri-Rad et al., 2021). However, a suitable version for *continuous* fiber reinforced polymer composites does not yet exist.

In continuous fiber reinforced polymers, fibers behave elastically until fracture, while the polymer matrix is responsible for the viscoelastic/viscoplastic response. Combined in a composite, this results in a mostly elastic response when loaded in fiber direction and in a viscoplastic response under off-axis loads. In a constitutive model, strong transverse isotropy can be achieved through the use of transversely isotropic stress invariants (Spencer, 1987; Eidel, 2004) for describing yield criteria, as previously done with Perzyna-type viscoplastic models (Koerber et al., 2018; Gerbaud et al., 2019; Rodrigues Lopes et al., 2022). These models have been successfully applied to the simulation of rate-dependent anisotropic plasticity in *thermosetting* polymer composites under short term loadings. As opposed to *thermosets*, *thermoplastics* lack primary (chemical) bonds between polymer chains (Brinson and Brinson, 2015). When subjected to stress, the polymer response transitions from solid-like to fluid-like, which is described in the EGP model with an Eyring-type non-Newtonian flow rule. With the non-Newtonian flow rule, creep and rate-dependent plasticity are treated in a unified manner. In addition, the effects of temperature can be taken into account through the Eyring relation, as well as the effects of pressure (Govaert et al., 2000, 2001) and aging (Klompen et al., 2005).

In this manuscript, we combine the use of transversely isotropic invariants and non-Newtonian flow, and propose an invariant-based mesoscopic extension of the EGP model for simulating rate-dependent plasticity and creep in continuous fiber reinforced thermoplastic composites. For assessing the accuracy of the mesoscopic constitutive model, a detailed micromodel of a carbon/PEEK composite (Kovačević and van der Meer, 2022; Kovačević et al., 2022) is used with fibers and matrix explicitly modeled. The micromodel first serves to identify the parameters of the mesoscopic constitutive model through numerical homogenization (Van Der Meer, 2016; Daghia et al., 2023; Liu et al., 2020) with a parameter identification procedure based on a few stress–strain curves. Subsequently, the response of the mesoscale model under off-axis constant strain rates and creep loads is assessed. Finally, unidirectional plies subjected to off-axis strain rates are simulated and compared against experiments.
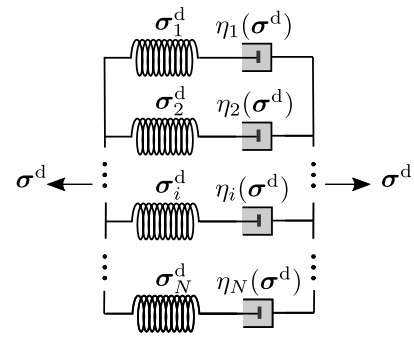

Fig. 1. Rheological model of the driving stress.

Scalars are represented by italic symbols (*e.g. a*), while vectors are denoted using italic bold lower case symbols (*e.g. a*). Second-order tensors are expressed with bold upper case Roman symbols (*e.g.* **A**), and fourth-order tensors are indicated by bold blackboard symbols (*e.g.* $\mathbb{A}$). The symmetric and skew-symmetric parts of a second order tensor **A** are given by $\mathbf{A}^{\text{sym}} = 1/2 \left(\mathbf{A} + \mathbf{A}^{\text{T}} \right)$ and $\mathbf{A}^{\text{skw}} = 1/2 \left(\mathbf{A} - \mathbf{A}^{\text{T}} \right)$. The product of two second-order tensors **A** and **B** is expressed as $\mathbf{A} \cdot \mathbf{B} = A_{ik} B_{kj}$, while the double contraction is given by $\mathbf{A} : \mathbf{B} = A_{ij} B_{ij}$. Finally, the dyadic product of two vectors *a* and *b* is written as $\boldsymbol{a} \otimes \boldsymbol{b} = a_i b_j$.

2. Formulation of the constitutive model

The mesoscopic constitutive model for the composite material is based on the EGP model for neat polymers (Tervoort et al., 1996, 1998; Van Breemen et al., 2011), which assumes two contributions to the stress: a driving stress $\boldsymbol{\sigma}^{\text{d}}$ and a hardening stress $\boldsymbol{\sigma}^{\text{h}}$

$$\boldsymbol{\sigma} = \boldsymbol{\sigma}^{\text{d}} + \boldsymbol{\sigma}^{\text{h}} \tag{1}$$

The driving stress is described by a spectrum of relaxation times, which is incorporated in the model by adding N nonlinear spring-dashpots (denoted as *modes*) in parallel. The driving stress is the sum of the driving stresses $\boldsymbol{\sigma}_i^{\text{d}}$ in each mode i

$$\boldsymbol{\sigma}^{\text{d}} = \sum_i^N \boldsymbol{\sigma}_i^{\text{d}} \tag{2}$$

For thermorheologically simple materials, it can be assumed that the viscosity of each mode η_i has the same functional dependence on the *total* driving stress $\boldsymbol{\sigma}^{\text{d}}$ (Tervoort et al., 1996). The rheological model of the driving stress contribution is shown in Fig. 1.

In this manuscript, the focus is on the driving stress contribution for describing anisotropic rate-dependent plasticity in the pre-yield and yield regime. Therefore, the hardening contribution is not taken into account ($\boldsymbol{\sigma}^{\text{h}} = 0$). To improve readability, the superscript (d) in the driving stress is dropped in the remainder of the text.

2.1. Kinematics

In each mode i, a multiplicative decomposition of the total deformation gradient **F** into an elastic $\mathbf{F}_{\text{e}i}$ and a plastic $\mathbf{F}_{\text{p}i}$ deformation gradient is assumed (Kröner, 1959; Lee, 1969)

$$\mathbf{F} = \mathbf{F}_{\text{e}i} \cdot \mathbf{F}_{\text{p}i} \tag{3}$$

The plastic deformation gradient maps the neighborhood of a mesoscopic material point from the *initial* configuration Ω_0 to a fictitious, locally stress-free, *intermediate* configuration $\hat{\Omega}_i$. Subsequently, the elastic deformation maps it from the *intermediate* configuration to the

Major symbols

Variable	Type	Meaning
General		
θ_0	Scalar	Initial off-axis angle
θ	Scalar	Off-axis angle
ε	Scalar	True strain
σ	Scalar	True stress
ε_{eng}	Scalar	Engineering strain
σ_{eng}	Scalar	Engineering stress
S	2nd order tensor	2nd Piola Kirchhoff-stress
F	2nd order tensor	Deformation gradient
C	2nd order tensor	Right Cauchy–Green tensor
B	2nd order tensor	Left Cauchy–Green tensor
All modes		
N	Scalar	Number of modes
μ_{p}	Scalar	Pressure dependency parameter
σ_0	Scalar	Nonlinearity parameter
η_0	Scalar	Maximum initial viscosity
α_2	Scalar	Anisotropy parameter
$\bar{\sigma}$	Scalar	Total equivalent stress
a_σ	Scalar	Stress shift factor
I_1, I_2, I_3	Scalars	Transversely isotropic invariants
$\boldsymbol{a}_0$	Vector	Fiber vector in initial configuration
$\boldsymbol{a}$	Vector	Fiber vector in current configuration
$\bar{\boldsymbol{a}}$	Vector	Normalized fiber vector in current configuration
$\bar{A}$	2nd order tensor	Structural tensor in current configuration
$\boldsymbol{\sigma}$	2nd order tensor	Cauchy stress
$\boldsymbol{\sigma}^{\text{pind}}$	2nd order tensor	Plasticity inducing Cauchy stress
$\mathbb{P}$	4th order tensor	Tensor that maps $\boldsymbol{\sigma}$ to $\boldsymbol{\sigma}^{\text{pind}}$
Mode i		
$\bar{\Sigma}_i$	Scalar	Equivalent stress
$\dot{\gamma}_{\text{p}i}$	Scalar	Equivalent rate of plastic deformation
m_i	Scalar	Ratio of elastic constants in relaxation spectrum
η_i	Scalar	Stress-dependent viscosity
η_{0i}	Scalar	Initial viscosity
$\lambda_i, \mu_i, \alpha_i, \beta_i, \gamma_i$	Scalars	Hyperelastic model parameters
$\hat{I}_{1i}, \hat{I}_{2i}, \hat{I}_{3i}$	Scalars	Transversely isotropic invariants
$\hat{\boldsymbol{a}}_i$	Vector	Fiber vector in intermediate configuration
$\mathbf{F}_{\text{p}i}$	2nd order tensor	Plastic deformation gradient
$\mathbf{F}_{\text{e}i}$	2nd order tensor	Elastic deformation gradient
$\hat{A}_i$	2nd order tensor	Structural tensor in intermediate configuration
$\hat{\mathbf{L}}_{\text{p}i}$	2nd order tensor	Plastic velocity gradient
$\hat{\mathbf{D}}_{\text{p}i}$	2nd order tensor	Rate of plastic deformation
$\hat{\mathbf{W}}_{\text{p}i}$	2nd order tensor	Plastic material spin
$\hat{\mathbf{N}}_{\text{p}i}$	2nd order tensor	Plastic normal
$\hat{\mathbf{B}}_{\text{e}i}$	2nd order tensor	Elastic left Cauchy–Green tensor
$\hat{\mathbf{C}}_{\text{e}i}$	2nd order tensor	Elastic right Cauchy–Green tensor
$\boldsymbol{\sigma}_i$	2nd order tensor	Cauchy stress tensor
Σ_i	2nd order tensor	Mandel-like stress tensor
Σ_i^{sym}	2nd order tensor	Symmetric part of Mandel-like stress tensor
Σ_i^{pind}	2nd order tensor	Plasticity inducing Mandel-like stress tensor
$\hat{\mathbb{P}}_i$	4th order tensor	Tensor that maps Σ_i^{sym} to Σ_i^{pind}

current configuration Ω (see Fig. 2). The plastic velocity gradient in the *intermediate* configuration reads

$$\hat{\mathbf{L}}_{\text{p}i} = \dot{\mathbf{F}}_{\text{p}i} \cdot \mathbf{F}_{\text{p}i}^{-1} = \underbrace{\left(\dot{\mathbf{F}}_{\text{p}i} \cdot \mathbf{F}_{\text{p}i}^{-1}\right)^{\text{sym}}}_{\hat{\mathbf{D}}_{\text{p}i}} + \underbrace{\left(\dot{\mathbf{F}}_{\text{p}i} \cdot \mathbf{F}_{\text{p}i}^{-1}\right)^{\text{skw}}}_{\hat{\mathbf{W}}_{\text{p}i}} \tag{4}$$

where $\hat{\mathbf{D}}_{\text{p}i}$ is the *rate of plastic deformation* and $\hat{\mathbf{W}}_{\text{p}}$ is the *plastic material spin* (Dafalias, 1998). To overcome the non-uniqueness of the multiplicative decomposition with regards to the orientation of the *intermediate* configuration, we choose $\hat{\mathbf{W}}_{\text{p}i} = \mathbf{0}$ (Boyce et al., 1989,

1992). Therefore, the evolution of $\mathbf{F}_{\text{p}i}$ is described with the following differential equation

$$\dot{\mathbf{F}}_{\text{p}i} = \hat{\mathbf{D}}_{\text{p}i} \cdot \mathbf{F}_{\text{p}i} \tag{5}$$

The transverse isotropy that originates from the microstructure of the unidirectional polymer composite is characterized by fiber direction vectors $\boldsymbol{a}_0$, $\hat{\boldsymbol{a}}_i$ and $\boldsymbol{a}$ in the *initial*, *intermediate* and *current* configurations, respectively. In the present mesoscopic constitutive model, the fiber vector represents *continuous* fibers in the composite and is
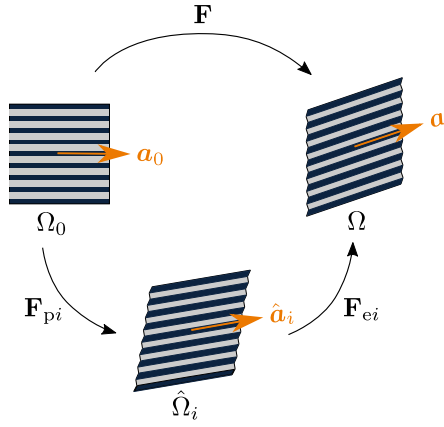
Fig. 2. Decomposition of total deformation in elastic and plastic deformation for *each* mode i, with the corresponding *initial* Ω_0, *intermediate* $\hat{\Omega}_i$ and *current* configuration Ω.

assumed to remain affinely attached to the material during deformation,[1] which is described by the following transformations using the multiplicative decomposition in Eq. (3):

$$\boldsymbol{a} = \mathbf{F}_{\mathrm{e}i} \cdot \hat{\boldsymbol{a}}_i = \mathbf{F}_{\mathrm{e}i} \cdot \mathbf{F}_{\mathrm{p}i} \cdot \boldsymbol{a}_0 = \mathbf{F} \cdot \boldsymbol{a}_0 \tag{6}$$

Furthermore, plastic deformation is assumed to be isochoric:

$$\det\left(\mathbf{F}_{\mathrm{p}i}\right) = 1 \tag{7}$$

2.2. Viscoplasticity relations

The rate of plastic deformation in the intermediate configuration in each mode i follows a non-Newtonian flow rule

$$\hat{\mathbf{D}}_{\mathrm{p}i} = \dot{\gamma}_{\mathrm{p}i} \hat{\mathbf{N}}_{\mathrm{p}i} \tag{8}$$

where $\dot{\gamma}_{\mathrm{p}i}$ is the (scalar) equivalent plastic strain rate and $\hat{\mathbf{N}}_{\mathrm{p}i}$ is the direction of plastic flow. The equivalent plastic strain rate is given by

$$\dot{\gamma}_{\mathrm{p}i} = \frac{\bar{\Sigma}_i}{\eta_i} \tag{9}$$

where $\bar{\Sigma}_i$ is the equivalent stress in mode i. The viscosity η_i is determined as

$$\eta_i = \eta_{0i} \, a_\sigma \tag{10}$$

where a_σ is the *stress shift factor*[2] and η_{0i} is the initial viscosity of mode i. The *stress shift factor* follows an Eyring relation and is a function of the *total* driving stress $\boldsymbol{\sigma}$ through a *total* equivalent stress $\bar{\sigma}$ and may depend on the temperature, pressure and aging (Govaert et al., 2000, 2001; Klompen and Govaert, 1999). Neglecting these influences, the *stress shift factor* reads

$$a_\sigma = \frac{\bar{\sigma}/\sigma_0}{\sinh\left(\bar{\sigma}/\sigma_0\right)} \tag{11}$$

where σ_0 is a parameter that controls the stress-induced exponential decrease of the viscosity. Note that the viscosity in each mode is different because of the different initial viscosities $\{\eta_{0i}\}$. However, a_σ is

the same across all modes, representing a thermorheologically simple material (Tervoort et al., 1996).

For describing plastic flow, a Mandel-like stress tensor (Mandel, 1972) is introduced as

$$\boldsymbol{\Sigma}_i = \mathbf{F}_{\mathrm{e}i}^{\mathrm{T}} \cdot \boldsymbol{\sigma}_i \cdot \mathbf{F}_{\mathrm{e}i}^{-\mathrm{T}} \tag{12}$$

which is work-conjugate to $\hat{\mathbf{D}}_{\mathrm{p}i}$ and is in general not symmetric for anisotropic materials (Lubliner, 2008). To ensure a symmetric $\hat{\mathbf{D}}_{\mathrm{p}i}$ and to remain consistent with the choice of a vanishing $\hat{\mathbf{W}}_{\mathrm{p}i}$ (see Section 2.1), it is assumed that *only* the symmetric part of $\boldsymbol{\Sigma}_i$ determines the plastic flow direction (Rodrigues Lopes et al., 2022; Eidel, 2004; Dean et al., 2016), *i.e.*

$$\hat{\mathbf{N}}_{\mathrm{p}i} = \frac{\partial \bar{\Sigma}_i}{\partial \boldsymbol{\Sigma}_i^{\mathrm{sym}}} \tag{13}$$

In the (original) isotropic EGP model, the equivalent stress(es) are proportional to the Von Mises stress (Tervoort et al., 1996, 1998; Govaert et al., 2000; Klompen et al., 2005; Van Breemen et al., 2011). For *short* and *long* fiber reinforced polymer composites, they can be proportional to the Hill effective stress (Amiri-Rad et al., 2019; Amiri-Rad et al., 2021). In this work, strong transverse isotropy of *continuous* fiber reinforced polymer composites is taken into account by defining the equivalent stresses $\bar{\sigma}$ and $\bar{\Sigma}_i$ as functions of transversely isotropic stress invariants. In addition, anisotropic pressure dependency is incorporated by modifying the Eyring-type relation Eq. (11). The invariant-based formulation is presented in the next section.

2.3. Invariant formulation

Fiber reinforced polymer composites can be considered transversely isotropic at the mesoscale. The response of the mesoscopic constitutive model should therefore be invariant with respect to the symmetry transformations for transverse isotropy (Boehler, 1987). For unidirectional fiber reinforced polymer composites with strong anisotropy, additional requirements can be specified: (*i*) the material should not flow in the direction of the fiber, (*ii*) the plastic deformation should be isochoric (as stated in Eq. (7)) and (*iii*) the pressure dependence of the polymer matrix should be taken into account. These requirements can be satisfied by using transversely isotropic invariants (Spencer, 1972; Boehler, 1987) for defining the equivalent stresses $\bar{\sigma}$ and $\bar{\Sigma}_i$ and by extending the Eyring relation (Eq. (11)) to account for anisotropic pressure dependence.

2.3.1. Total equivalent stress

The material symmetries of the fiber reinforced polymer composite are represented with fiber direction (unit) vectors $\boldsymbol{a}_0$ and $\bar{\boldsymbol{a}} = \boldsymbol{a}/\|\boldsymbol{a}\|$ in the *initial* and *current* configurations, respectively (see Fig. 2). Furthermore, the stress is first split into a plasticity inducing $\boldsymbol{\sigma}^{\mathrm{pind}}$ and a remaining (elastic) part (Spencer, 1972, 1987)

$$\boldsymbol{\sigma}^{\mathrm{pind}} = \boldsymbol{\sigma} - \left(p\,\mathbf{I} + \sigma_{\mathrm{f}}\,\bar{\mathbf{A}}\right) \tag{14}$$

where p is the pressure, σ_{f} the part of the stress projection onto the fiber direction that exceeds the pressure and $\bar{\mathbf{A}} = \bar{\boldsymbol{a}} \otimes \bar{\boldsymbol{a}}$. The plasticity inducing stress can be determined from the total stress $\boldsymbol{\sigma}$ with the mapping

$$\boldsymbol{\sigma}^{\mathrm{pind}} = \mathbb{P} : \boldsymbol{\sigma} \tag{15}$$

where $\mathbb{P}$ is a fourth order tensor, given as

$$\mathbb{P} = \mathbb{I} - \frac{1}{2}\mathbf{I} \otimes \mathbf{I} - \frac{3}{2}\bar{\mathbf{A}} \otimes \bar{\mathbf{A}} + \frac{1}{2}\left(\bar{\mathbf{A}} \otimes \mathbf{I} - \mathbf{I} \otimes \bar{\mathbf{A}}\right) \tag{16}$$

with $\mathbb{I}_{ijkl} = \delta_{ik}\delta_{jl}$. The following three transversely isotropic invariants are introduced (Vogler et al., 2013)

$$I_1 = \frac{1}{2}\mathrm{tr}\left[\boldsymbol{\sigma}^{\mathrm{pind}} \cdot \boldsymbol{\sigma}^{\mathrm{pind}}\right] - \bar{\boldsymbol{a}} \cdot \left[\boldsymbol{\sigma}^{\mathrm{pind}} \cdot \boldsymbol{\sigma}^{\mathrm{pind}}\right] \cdot \bar{\boldsymbol{a}} \tag{17}$$

$$I_2 = \bar{\boldsymbol{a}} \cdot \left[\boldsymbol{\sigma}^{\mathrm{pind}} \cdot \boldsymbol{\sigma}^{\mathrm{pind}}\right] \cdot \bar{\boldsymbol{a}} \tag{18}$$

---

[1] For short fiber composites, this assumption is debatable as pointed out by Ref. Dafalias (1998), where short fibers may evolve differently from the mesoscopic kinematics.

[2] The name *stress shift factor* refers to its effect of reducing the initial viscosity with increasing stress, resulting in horizontal shifts at different stress levels in creep-compliance curves on logarithmic time scales (Tervoort et al., 1998).
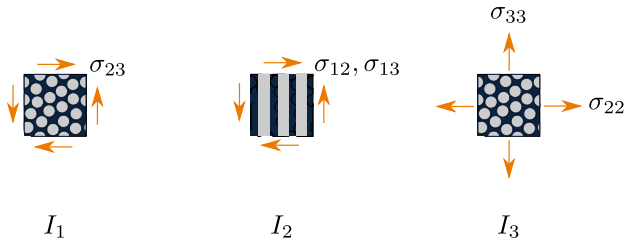
I_1 I_2 I_3

Fig. 3. The transversely isotropic stress invariants are related to transverse shear (*left*), longitudinal shear (*middle*) and biaxial tension or compression (*right*).

$$I_3 = \mathrm{tr}\,[\boldsymbol{\sigma}] - \bar{\boldsymbol{a}} \cdot \boldsymbol{\sigma} \cdot \bar{\boldsymbol{a}} \tag{19}$$

To inspect the meaning of these invariants, they can be expressed in terms of stress components in a local frame, where $\boldsymbol{e}_1$ is aligned with the fiber direction vector $\boldsymbol{a}$:

$$I_1 = \frac{1}{4}\left(\sigma_{22} - \sigma_{33}\right)^2 + \sigma_{23}^2 \tag{20}$$

$$I_2 = \sigma_{12}^2 + \sigma_{13}^2 \tag{21}$$

$$I_3 = \sigma_{22} + \sigma_{33} \tag{22}$$

From Eq. (20)–(22), it can be seen that I_1 is related to transverse shear, I_2 to longitudinal shear and I_3 to biaxial tension or compression in the transverse plane (see Fig. 3).[3] With these invariants, an equivalent stress can be constructed that does not induce yielding due to stress projections in the fiber direction. The *total* equivalent stress $\bar{\sigma}$ that drives the evolution of the viscosity through *stress shift factor* a_σ is proposed as

$$\bar{\sigma} = \sqrt{2\left(I_1 + \alpha_2 I_2\right)} \tag{23}$$

where α_2 is a model parameter. The equivalent stress $\bar{\sigma}$ is a measure for shear stress in the polymer matrix, reflecting that for continuous fiber reinforced polymer composites, transverse shear (invariant I_1) and longitudinal shear (invariant I_2) do not lead to the same shear stresses in the polymer matrix, hence demanding the coefficient α_2.

The third invariant I_3 is used to describe pressure dependence of the polymer matrix, by extending the Eyring relation Eq. (11) as

$$a_\sigma = \frac{\bar{\sigma}/\sigma_0}{\sinh\left(\bar{\sigma}/\sigma_0\right)} \exp\left(-\mu_\mathrm{p} \frac{I_3}{\sigma_0}\right) \tag{24}$$

where μ_p is a pressure dependency parameter. This relation is similar to previous modifications of the Eyring relation for isotropic polymers (Govaert et al., 2000, 2001; Klompen et al., 2005), where instead of I_3, the hydrostatic pressure $p = -1/3\,\mathrm{tr}\,\boldsymbol{\sigma}$ was used in the argument of the exponential function. Note that through I_3 (which is a measure for pressure in the polymer matrix), anisotropic pressure dependence of the composite is taken into account with Eq. (24).

2.3.2. Equivalent stress of each mode

As mentioned in Section 2.2, the equivalent stress of each mode $\bar{\Sigma}_i$ is a function of the symmetric part of $\boldsymbol{\Sigma}_i$ and the fiber direction vector in the *intermediate* configuration $\hat{\boldsymbol{a}}_i$. Replacing in Eqs. (15) and (16) quantities referring to the *current* configuration $\{\boldsymbol{\sigma}, \boldsymbol{a}\}$ by quantities referring to the *intermediate* configuration $\{\boldsymbol{\Sigma}_i^{\mathrm{sym}}, \hat{\boldsymbol{a}}_i\}$, gives the plasticity inducing part of $\boldsymbol{\Sigma}_i^{\mathrm{sym}}$

$$\boldsymbol{\Sigma}_i^{\mathrm{pind}} = \hat{\mathbb{P}}_i : \boldsymbol{\Sigma}_i^{\mathrm{sym}} \tag{25}$$

---

[3] Note that these invariants are not the same as in classical plasticity theory for $\{I_i\}_{i=1,2,3}$. Here we follow the definitions from Refs. Eidel (2004), Vogler et al. (2013), Dean et al. (2016), Koerber et al. (2018), Gerbaud et al. (2019) and Rodrigues Lopes et al. (2022).

with corresponding fourth order tensor $\hat{\mathbb{P}}_i$

$$\hat{\mathbb{P}}_i = \mathbb{I} - \frac{1}{2}\mathbf{I} \otimes \mathbf{I} - \frac{3}{2}\hat{\mathbf{A}}_i \otimes \hat{\mathbf{A}}_i + \frac{1}{2}\left(\hat{\mathbf{A}}_i \otimes \mathbf{I} - \mathbf{I} \otimes \hat{\mathbf{A}}_i\right) \tag{26}$$

and invariants for each mode i

$$\hat{I}_{1i} = \frac{1}{2}\,\mathrm{tr}\left[\boldsymbol{\Sigma}_i^{\mathrm{pind}} \cdot \boldsymbol{\Sigma}_i^{\mathrm{pind}}\right] - \hat{\boldsymbol{a}}_i \cdot \left[\boldsymbol{\Sigma}_i^{\mathrm{pind}} \cdot \boldsymbol{\Sigma}_i^{\mathrm{pind}}\right] \cdot \hat{\boldsymbol{a}}_i \tag{27}$$

$$\hat{I}_{2i} = \hat{\boldsymbol{a}}_i \cdot \left[\boldsymbol{\Sigma}_i^{\mathrm{pind}} \cdot \boldsymbol{\Sigma}_i^{\mathrm{pind}}\right] \cdot \hat{\boldsymbol{a}}_i \tag{28}$$

To prevent plastic flow in fiber direction and account for plastic incompressibility, only invariants $\hat{I}_{1i}$ and $\hat{I}_{2i}$, which are functions of $\boldsymbol{\Sigma}_i^{\mathrm{pind}}$, are used to describe the direction of plastic flow through Eq. (13). Similar to the *total* equivalent stress $\bar{\sigma}$, the equivalent stress of mode i is defined as

$$\bar{\Sigma}_i = \sqrt{2\left(\hat{I}_{1i} + \alpha_2 \hat{I}_{2i}\right)} \tag{29}$$

with plastic normal direction

$$\mathbf{N}_{\mathrm{p}i} = \frac{\partial \bar{\Sigma}_i}{\partial \boldsymbol{\Sigma}_i^{\mathrm{sym}}} = \frac{1}{\bar{\Sigma}_i}\left[\frac{\partial \hat{I}_{1i}}{\partial \boldsymbol{\Sigma}_i^{\mathrm{sym}}} + \alpha_2 \frac{\partial \hat{I}_{2i}}{\partial \boldsymbol{\Sigma}_i^{\mathrm{sym}}}\right] \tag{30}$$

where α_2 is the same model parameter as in Eq. (23), to limit the number of parameters and aid their identification procedure. The derivatives of the invariants read

$$\frac{\partial \hat{I}_{1i}}{\partial \boldsymbol{\Sigma}_i^{\mathrm{sym}}} = \left[\left(\mathbf{I} - \hat{\mathbf{A}}_i\right) \cdot \boldsymbol{\Sigma}_i^{\mathrm{pind}} - \boldsymbol{\Sigma}_i^{\mathrm{pind}} \cdot \hat{\mathbf{A}}_i\right] : \hat{\mathbb{P}}_i \tag{31}$$

$$\frac{\partial \hat{I}_{2i}}{\partial \boldsymbol{\Sigma}_i^{\mathrm{sym}}} = \left[\hat{\mathbf{A}}_i \cdot \boldsymbol{\Sigma}_i^{\mathrm{pind}} + \boldsymbol{\Sigma}_i^{\mathrm{pind}} \cdot \hat{\mathbf{A}}_i\right] : \hat{\mathbb{P}}_i \tag{32}$$

Remark 1. The *total* equivalent stress $\bar{\sigma}$ is a function of $\boldsymbol{\sigma}$ and $\bar{\boldsymbol{a}}$, instead of $\boldsymbol{\Sigma}_i$ and $\hat{\boldsymbol{a}}_i$. The reason for this is that the latter quantities refer to an *intermediate* configuration, which is different for each mode (see Fig. 2). Therefore, 'total versions' of $\boldsymbol{\Sigma}$ and $\hat{\boldsymbol{a}}$ do not exist.

Remark 2. In the present contribution, thermorheologically simple material behavior is assumed. The model can be extended to simulate thermorheologically complex behavior with several relaxation processes. A multiprocess model can be obtained by adding multiple driving stress contributions in parallel, where each contribution obeys an Eyring relation with a different parameter σ_0 (Klompen and Govaert, 1999) and a different relaxation spectrum.

Remark 3. As pointed out by Van Der Meer (2016), the difference between stress combinations $\sigma_{12} - \sigma_{22}$ and $\sigma_{12} - \sigma_{33}$ is not considered in the invariant formulation. Furthermore, the effect on the yielding of a stress in fiber direction is removed. Although the material should not flow in the fiber direction, the stress in the fiber direction should contribute to the yielding of the polymer matrix under combined loading, for example longitudinal shear and stress in fiber direction. These assumptions remain limitations of the present mesoscale model.

Remark 4. In the equivalent stress definitions, only α_2 is used as a coefficient of invariant I_2. The fact that α_2 is cancelled in a transverse uniaxial tension and compression test simplifies the parameter identification procedure as will be shown in Section 3.

2.4. Embedded hyperelastic constitutive relations

A hyperelastic transversely isotropic constitutive model (Bonet and Burton, 1998) is used in this work to compute the stress in the composite material. The second Piola Kirchhoff stress $\mathbf{S}$ is decomposed in an isotropic (iso) and a transversely isotropic part (trn) as

$$\mathbf{S} = \mathbf{S}_{\mathrm{iso}} + \mathbf{S}_{\mathrm{trn}} \tag{33}$$

Without plastic deformations, these contributions are given as

$$\mathbf{S}_{\text{iso}} = \mu(\mathbf{I} - \mathbf{C}^{-1}) + \lambda J(J-1)\mathbf{C}^{-1}$$

$$\mathbf{S}_{\text{trn}} = 2\beta(\xi_2 - 1)\mathbf{I} + 2\left[\alpha + \beta(\xi_1 - 3) + 2\gamma(\xi_2 - 1)\right]\boldsymbol{a}_0 \otimes \boldsymbol{a}_0 \tag{34}$$
$$- \alpha\left(\mathbf{C} \cdot \boldsymbol{a}_0 \otimes \boldsymbol{a}_0 + \boldsymbol{a}_0 \otimes \mathbf{C} \cdot \boldsymbol{a}_0\right)$$

where $\mathbf{C} = \mathbf{F}^{\text{T}} \cdot \mathbf{F}$ is the right Cauchy–Green deformation tensor and $J = \det(\mathbf{F})$. The parameters $\lambda, \mu, \alpha, \beta$ and γ are material constants that can be computed from the Young moduli and the Poisson ratios

$$n = \frac{E_{22}}{E_{11}}$$

$$m = 1 - v_{21} - 2nv_{21}^2$$

$$\lambda = E_{22}\frac{v_{21} + n\,v_{21}^2}{m(1+v_{21})}$$

$$\mu = \frac{E_{22}}{2(1+v_{21})} \tag{35}$$

$$\alpha = \mu - G_{12}$$

$$\beta = \frac{E_{22}\,v_{21}^2(1-n)}{4\,m(1+v_{21})}$$

$$\gamma = \frac{E_{11}(1-v_{21})}{8\,m} - \frac{\lambda+2\mu}{8} + \frac{\alpha}{2} - \beta$$

where the Young moduli E_{11} and E_{22}, the shear modulus G_{12} and the Poisson ratio v_{21} refer to a local coordinate frame with e_1 aligned with the fiber direction. Furthermore, ξ_1 and ξ_2 are defined as

$$\xi_1 = \text{tr}(\mathbf{C}) \tag{36}$$

$$\xi_2 = \boldsymbol{a} \cdot \boldsymbol{a} \tag{37}$$

In the present contribution, we use this hyperelastic transversely isotropic constitutive model to compute the stress in each mode i when the material is mapped from its *intermediate* configuration to the *current* configuration (see Fig. 2). To this end, the following quantities are replaced by quantities that refer to the *intermediate* configurations: $\{\mathbf{S}, \boldsymbol{a}_0, \mathbf{C}, \xi_1, J\} \rightarrow \{\hat{\mathbf{S}}_i, \hat{\boldsymbol{a}}_i, \mathbf{C}_{ei}, \xi_{1ei}, J_{ei}\}$. The relations for the hyperelastic model of each mode i become

$$\hat{\mathbf{S}}_{\text{iso},i} = \mu_i(\mathbf{I} - \mathbf{C}_{ei}^{-1}) + \lambda_i J_{ei}(J_{ei}-1)\mathbf{C}_{ei}^{-1}$$

$$\hat{\mathbf{S}}_{\text{trn},i} = 2\beta_i(\xi_2 - 1)\mathbf{I} + 2\left[\alpha_i + \beta_i(\xi_{1ei} - 3) + 2\gamma_i(\xi_2 - 1)\right]\hat{\boldsymbol{a}}_i \otimes \hat{\boldsymbol{a}}_i \tag{38}$$
$$- \alpha_i\left(\mathbf{C}_{ei} \cdot \hat{\boldsymbol{a}}_i \otimes \hat{\boldsymbol{a}}_i + \hat{\boldsymbol{a}}_i \otimes \mathbf{C}_{ei} \cdot \hat{\boldsymbol{a}}_i\right)$$

Note that each mode has a different set of elastic constants. Furthermore, the vector $\hat{\boldsymbol{a}}_i$ is a unit vector since plastic flow is excluded in fiber direction. Pushing forward Eq. (38) from the *intermediate* to the *current* configuration gives the Cauchy stress contributions

$$\sigma_{\text{iso},i} = \frac{\mu_i}{J_{ei}}\left(\mathbf{B}_{ei} - \mathbf{I}\right) + \lambda_i(J_{ei}-1)\mathbf{I}$$

$$J_{ei}\sigma_{\text{trn},i} = 2\beta_i(\xi_2 - 1)\mathbf{B}_{ei} + 2\left[\alpha_i + \beta_i(\xi_{1ei} - 3) + 2\gamma_i(\xi_2 - 1)\right]\boldsymbol{a} \otimes \boldsymbol{a} \tag{39}$$
$$- \alpha_i\left(\mathbf{B}_{ei} \cdot \boldsymbol{a} \otimes \boldsymbol{a} + \boldsymbol{a} \otimes \mathbf{B}_{ei} \cdot \boldsymbol{a}\right)$$

where $\mathbf{B}_{ei} = \mathbf{F}_{ei} \cdot \mathbf{F}_{ei}^{\text{T}}$ is the elastic right Cauchy–Green deformation tensor. Note that the kinematics in Fig. 2, with re-orienting fiber direction vector(s) in the *intermediate* configuration(s), are taken into account in the embedded hyperelastic model.

2.5. Multimode model

Direction-, pressure- and rate-dependent yielding can be described by a single mode (see Fig. 4), requiring four parameters: α_2, μ_{p}, σ_0 and η_0. However, for polymers and polymer composites, a single viscosity is not sufficient to describe the nonlinear response prior to yielding (Tervoort et al., 1996; Van Breemen et al., 2011). A more accurate representation of the time-dependent pre-yield (and creep) response is obtained by including multiple modes (see Fig. 4). With N modes, the yield stress is then determined by the mode with the highest initial viscosity $\eta_0 = \max\{\eta_{0i}\}$.
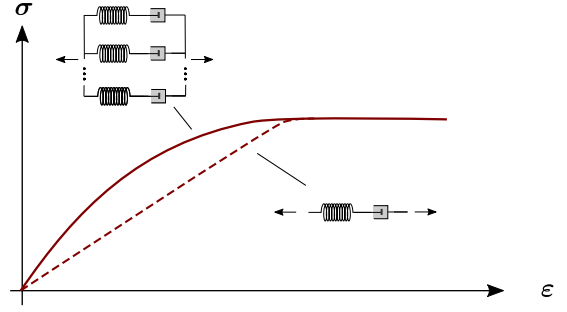

Fig. 4. Stress–strain response with a single mode and with multiple modes.

A relaxation spectrum can be determined from a single stress–strain curve, obtained from a test under a constant strain rate as described in Ref. Van Breemen et al. (2011). This procedure was originally developed for isotropic polymers and recently extended to anisotropic yielding in *short*- and *long*-fiber composites (Amiri-Rad et al., 2019). The same procedure is applied to the present model for *continuous* fiber reinforced polymer composites and is briefly outlined here for completeness. For more details, the reader is referred to the Refs. Van Breemen et al. (2011) and Amiri-Rad et al. (2019).

The method makes use of a Boltzmann integral with N unknown relaxation times to fit a 1D equivalent stress–strain curve from a constant strain rate test under off-axis angle θ. The result of the procedure is a spectrum of moduli $\{E_{\theta i}\}$ and initial viscosities $\{\eta_{0i}\}$. It is then assumed that the ratio

$$m_i = \frac{E_{\theta i}}{\sum_i^N E_{\theta i}} \tag{40}$$

is the same for E_{11}, E_{22} and G_{12}. With the set of ratios $\{m_i\}$, the elastic constants are obtained for each mode

$$E_{11i} = m_i E_{11}$$

$$E_{22i} = m_i E_{22}$$

$$G_{12i} = m_i G_{12} \tag{41}$$

$$v_{21i} = v_{21}$$

The hyperelastic parameters for each mode are obtained with Eq. (35), replacing constants $\{E_{11}, E_{22}, G_{12}\}$ by $\{E_{11i}, E_{22i}, G_{12i}\}$.

2.6. Integration of the constitutive relations

To compute the stress in each mode from the elastic deformation, the plastic deformation must be known, which in turn depends, through the non-Newtonian flow rule, on the stress in each mode and on the *total* stress through the stress-dependent shift factor. This renders a nonlinear relation between the total stress and deformation gradient, that must be solved with an iterative scheme.

2.6.1. Nested scheme
Following Ref. Khaleghi et al. (2022), a nested scheme with an *external* and *internal* solution process is used (see Fig. 5). In the *external* scheme, the *stress shift factor* a_σ is iteratively solved with Newton iterations. For every *external* iteration, the viscosities $\{\eta_i\}$ of the modes are known, which allows for computing the stress in each mode σ_i separately with an *internal* Newton–Raphson scheme.

2.6.2. External Newton–Raphson scheme
For solving the *stress shift factor* a_σ, Eq. (24) is cast in residual form

$$R_{a_\sigma} = a_\sigma - \frac{\bar{\sigma}/\sigma_0}{\sinh(\bar{\sigma}/\sigma_0)}\exp\left(-\mu_{\text{p}}\frac{I_3}{\sigma_0}\right) \tag{42}$$
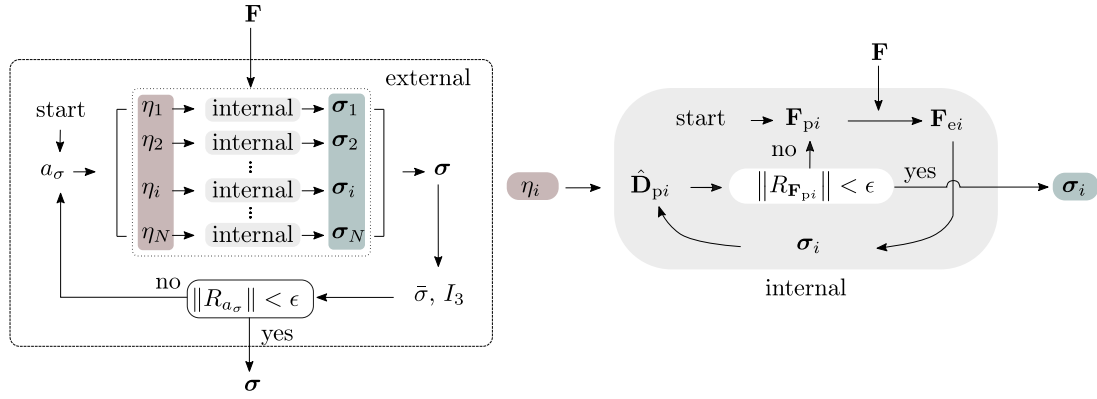
Fig. 5. Nested external–internal solution scheme. At every external iteration (*left*), N internal schemes are solved, one for each mode i (*right*).

The root of this equation is found with Newton iterations $j = 1 \ldots N_{\text{iter}}$ by updating a_σ as follows

$$a_\sigma^{(j+1)} = a_\sigma^{(j)} - \frac{R_{a_\sigma}^{(j)}}{\left. \frac{\partial R_{a_\sigma}}{\partial a_\sigma} \right|_{\mathbf{F}}^{(j)}} \tag{43}$$

where $\partial R_{a_\sigma} / \partial a_\sigma \big|_{\mathbf{F}}$ is the Jacobian for the *external* scheme, which is derived in Section 2.7.2. For each *external* Newton iteration j, the stress in each mode $\boldsymbol{\sigma}_i$ is found with the *internal* Newton–Raphson scheme, with viscosity $\eta_i^{(j)} = \eta_{0i} a_\sigma^{(j)}$. Subsequently, the *total equivalent stress* $\bar{\sigma}$ is computed and the residual R_{a_σ} and the Jacobian $\partial R_{a_\sigma} / \partial a_\sigma \big|_{\mathbf{F}}$ are evaluated to update the stress shift factor $a_\sigma^{(j+1)}$ for the next iteration with Eq. (43).

2.6.3. Internal Newton–Raphson scheme

In the *internal* scheme, the plastic deformation $\mathbf{F}_{\text{p}i}$ is chosen as primary unknown. The time integration of Eq. (5) is performed with an implicit exponential map (Eterovic and Bathe, 1990; Weber and Anand, 1990) to retain plastic incompressibility (Eq. (7)) (Sansour and Kollmann, 1998). The plastic deformation at the current time step $\mathbf{F}_{\text{p}i}$ is computed from the rate of plastic deformation at the current time step $\hat{\mathbf{D}}_{\text{p}i}$ and the plastic deformation at the previous time step $\mathbf{F}_{\text{p}i}^0$:

$$\mathbf{F}_{\text{p}i} = \exp\left(\hat{\mathbf{D}}_{\text{p}i} \Delta t \right) \cdot \mathbf{F}_{\text{p}i}^0 \tag{44}$$

where the tensor exponential function is replaced by a Padé approximation (Baaser, 2004)

$$\exp\left(\hat{\mathbf{D}}_{\text{p}i} \Delta t \right) \approx \boldsymbol{\Pi} \left(\hat{\mathbf{D}}_{\text{p}i}, \Delta t \right) = \left(\mathbf{I} - \frac{\Delta t}{2} \hat{\mathbf{D}}_{\text{p}i} \right)^{-1} \cdot \left(\mathbf{I} + \frac{\Delta t}{2} \hat{\mathbf{D}}_{\text{p}i} \right) \tag{45}$$

Casting this equation in residual form yields

$$\mathbf{R}_{\mathbf{F}_{\text{p},i}} = \mathbf{F}_{\text{p}i} - \boldsymbol{\Pi} \left(\Delta t, \hat{\mathbf{D}}_{\text{p}i} \right) \cdot \mathbf{F}_{\text{p}i}^0 \tag{46}$$

The root of this equation is solved by updating the plastic deformation for each *internal* iteration $k = 1 \ldots N_{\text{iter}}$ as follows

$$\mathbf{F}_{\text{p}i}^{(k+1)} = \mathbf{F}_{\text{p}i}^{(k)} - \left[\frac{\partial \mathbf{R}_{\mathbf{F}_{\text{p}i}}}{\partial \mathbf{F}_{\text{p}i}}^{(k)} \right]^{-1} : \mathbf{R}_{\mathbf{F}_{\text{p}i}}^{(k)} \tag{47}$$

where $\partial \mathbf{R}_{\mathbf{F}_{\text{p}i}} / \partial \mathbf{F}_{\text{p}i}$, is the Jacobian for the *internal* Newton–Raphson scheme, which is given in Section 2.7.1. With the plastic deformation $\mathbf{F}_{\text{p}i}$, the elastic deformation in each mode $\mathbf{F}_{\text{e}i}$ is computed with Eq. (3) and the stress $\boldsymbol{\sigma}_i$ with Eq. (39). Subsequently, the total equivalent stress $\bar{\sigma}$ is computed with Eq. (23), after which the *internal* residual $\mathbf{R}_{\mathbf{F}_{\text{p}i}}$ and Jacobian $\partial \mathbf{R}_{\mathbf{F}_{\text{p}i}} / \partial \mathbf{F}_{\text{p}i}$, are evaluated to update the plastic deformation for the next iteration with Eq. (47).

Remark 5. The time step dependence from the time integration scheme with Padé approximation, Eq. (46), is assessed in Section 5. For a better approximation of the exponential map, a higher-order Padé approximation (Baaser, 2004) could be used.

2.7. Jacobians

The Jacobians for the *internal* and *external* Newton–Raphson schemes and the consistent tangent modulus for the *global* implicit solution scheme are derived in this section.

2.7.1. Jacobian of the internal scheme

The Jacobian of the *internal* residual (Eq. (46)) reads

$$\frac{\partial \mathbf{R}_{\mathbf{F}_{\text{p}i}}}{\partial \mathbf{F}_{\text{p}i}} = \mathbb{I} + \frac{\partial \mathbf{R}_{\mathbf{F}_{\text{p}i}}}{\partial \boldsymbol{\Pi}_i} : \frac{\partial \boldsymbol{\Pi}_i}{\partial \hat{\mathbf{D}}_{\text{p}i}} : \left[\frac{\partial \hat{\mathbf{D}}_{\text{p}i}}{\partial \boldsymbol{\Sigma}_i^{\text{sym}}} : \frac{\partial \boldsymbol{\Sigma}_i^{\text{sym}}}{\partial \mathbf{F}_{\text{e}i}} : \frac{\partial \mathbf{F}_{\text{e}i}}{\partial \mathbf{F}_{\text{p}i}} + \frac{\partial \hat{\mathbf{D}}_{\text{p}i}}{\partial \hat{a}_i} \cdot \frac{\partial \hat{a}_i}{\partial \mathbf{F}_{\text{p}i}} \right] \tag{48}$$

The derivatives in this expression are given in Appendix A.

2.7.2. Jacobian of the external scheme

The Jacobian of the *external* residual (Eq. (42)) reads

$$\frac{\partial R_{a_\sigma}}{\partial a_\sigma} = 1 + \left[\frac{\partial R_{a_\sigma}}{\partial \bar{\sigma}} \frac{\partial \bar{\sigma}}{\partial \boldsymbol{\sigma}} + \frac{\partial R_{a_\sigma}}{\partial I_3} \frac{\partial I_3}{\partial \boldsymbol{\sigma}} \right] : \left[\sum_{i=1}^{N} \frac{\partial \boldsymbol{\sigma}_i}{\partial \mathbf{F}_{\text{e}i}} : \frac{\partial \mathbf{F}_{\text{e}i}}{\partial \mathbf{F}_{\text{p}i}} : \frac{\partial \mathbf{F}_{\text{p}i}}{\partial a_\sigma} \right] \tag{49}$$

where $\partial \bar{\sigma} / \partial \boldsymbol{\sigma}$ follows from Eq. (30) by replacing *intermediate* quantities $\{\bar{\Sigma}_i, \boldsymbol{\Sigma}^{\text{sym}}, \hat{I}_{1i}, \hat{I}_{2i}\}$ with *current* quantities $\{\bar{\sigma}, \boldsymbol{\sigma}, I_1, I_2\}$. The first and second terms in the sum on the RHS are given by Eqs. (A.19) and (A.12), respectively. The other terms are given in Appendix B. The terms $\{\partial \mathbf{F}_{\text{p}i} / \partial a_\sigma\}$ are obtained as follows. The *internal* residual for mode i is a function of independent variables a_σ and $\mathbf{F}_{\text{p}i}$. Therefore, the variation of the residual reads

$$\delta \mathbf{R}_{\mathbf{F}_{\text{p}i}} = \frac{\partial \mathbf{R}_{\mathbf{F}_{\text{p}i}}}{\partial a_\sigma} \delta a_\sigma + \frac{\partial \mathbf{R}_{\mathbf{F}_{\text{p}i}}}{\partial \mathbf{F}_{\text{p}i}} : \delta \mathbf{F}_{\text{p}i} \tag{50}$$

Since we solve iteratively for the root of $\mathbf{R}_{\mathbf{F}_{\text{p}i}}$ with the *internal* scheme, its variation between *external* iterations j vanishes, *i.e.* $\delta \mathbf{R}_{\mathbf{F}_{\text{p}i}} = \mathbf{0}$. This is a *consistency condition* that can be used for finding $\partial \mathbf{F}_{\text{p}i} / \partial a_\sigma$, similar to what is done in deriving consistent tangent moduli in classical plasticity models with return mapping schemes.

The *consistency condition* $\delta \mathbf{R}_{\mathbf{F}_{\text{p}i}} = \mathbf{0}$ gives, after rewriting, the sought-after derivative $\partial \mathbf{F}_{\text{p}i} / \partial a_\sigma$

$$\delta \mathbf{F}_{\text{p}i} = - \underbrace{\left[\frac{\partial \mathbf{R}_{\mathbf{F}_{\text{p}i}}}{\partial \mathbf{F}_{\text{p}i}} \right]^{-1} : \frac{\partial \mathbf{R}_{\mathbf{F}_{\text{p}i}}}{\partial a_\sigma} \delta a_\sigma}_{\frac{\partial \mathbf{F}_{\text{p}i}}{\partial a_\sigma}} \tag{51}$$

where the first term on the RHS is the Jacobian for the *internal* scheme (Eq. (48)). The second term on the RHS is given in Appendix B.
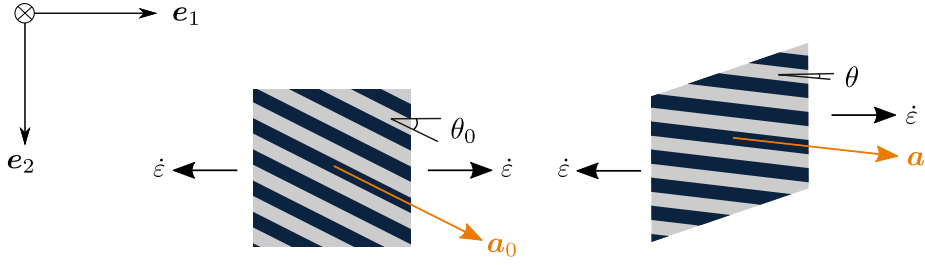
Fig. 6. Fiber reinforced polymer composite under off-axis tensile loading.

2.7.3. Consistent tangent modulus

The derivative of the Cauchy stress with respect to the deformation gradient reads

$$\frac{\partial \boldsymbol{\sigma}}{\partial \mathbf{F}} = \sum_i^N \left[\frac{\partial \boldsymbol{\sigma}_i}{\partial \mathbf{F}_{ei}} : \left(\frac{\partial \mathbf{F}_{ei}}{\partial \mathbf{F}} + \frac{\partial \mathbf{F}_{ei}}{\partial \mathbf{F}_{pi}} : \frac{\partial \mathbf{F}_{pi}}{\partial \mathbf{F}} \right) + \frac{\partial \boldsymbol{\sigma}_i}{\partial \boldsymbol{a}} \cdot \frac{\partial \boldsymbol{a}}{\partial \mathbf{F}} \right] \tag{52}$$

where $\partial \mathbf{F}_{ei}/\partial \mathbf{F}_{pi}$, $\partial \boldsymbol{\sigma}_i/\partial \mathbf{F}_e$ and $\partial \boldsymbol{\sigma}_i/\partial \boldsymbol{a}$ are given by Eq. (A.12), (A.19) and (C.3). The derivatives $\partial \mathbf{F}_{ei}/\partial \mathbf{F}$ and $\partial \boldsymbol{a}/\partial \mathbf{F}$ can be found by differentiating Equations (3) and (6). Furthermore, $\partial \mathbf{F}_{pi}/\partial \mathbf{F}$ in Eq. (52) reads

$$\frac{\partial \mathbf{F}_{pi}}{\partial \mathbf{F}} = \left. \frac{\partial \mathbf{F}_{pi}}{\partial \mathbf{F}} \right|_{a_\sigma} + \frac{\partial \mathbf{F}_{pi}}{\partial a_\sigma} \otimes \frac{\partial a_\sigma}{\partial \mathbf{F}} \tag{53}$$

where $\partial \mathbf{F}_{pi}/\partial a_\sigma$ is already given by Equations (51). Furthermore, $\left. \partial \mathbf{F}_{pi}/\partial \mathbf{F} \right|_{a_\sigma}$ is derived through an additional consistency condition of the *internal* scheme. For every fixed a_σ and varying $\mathbf{F}$, the internal residual for mode i vanishes between *global* iterations. Therefore

$$\delta \mathbf{R}_{\mathbf{F}_{pi}} = \frac{\partial \mathbf{R}_{\mathbf{F}_{pi}}}{\partial \mathbf{F}_{pi}} : \delta \mathbf{F}_{pi} + \frac{\partial \mathbf{R}_{\mathbf{F}_{pi}}}{\partial \mathbf{F}} : \delta \mathbf{F} = 0 \tag{54}$$

The derivative $\left. \partial \mathbf{F}_{pi}/\partial \mathbf{F} \right|_{a_\sigma}$ can be found by rewriting this expression

$$\delta \mathbf{F}_{pi} = \underbrace{ - \left[\frac{\partial \mathbf{R}_{\mathbf{F}_{pi}}}{\partial \mathbf{F}_{pi}} \right]^{-1} : \frac{\partial \mathbf{R}_{\mathbf{F}_{pi}}}{\partial \mathbf{F}} }_{\left. \frac{\partial \mathbf{F}_{pi}}{\partial \mathbf{F}} \right|_{a_\sigma}} : \delta \mathbf{F} = 0 \tag{55}$$

where the first term on the RHS is again the Jacobian of the *internal* residual (see Eq. (48)) and the second term on the RHS is given in Appendix C.

The third derivative $\partial a/\partial \mathbf{F}$ on the RHS of Eq. (53), which is the same for each mode, is obtained with a single *consistency condition* of the *external* scheme. At every *global* iteration, the *external* residual vanishes. Therefore

$$\delta R_{a_\sigma} = \frac{\partial R_{a_\sigma}}{\partial \mathbf{F}} : \delta \mathbf{F} + \frac{\partial R_{a_\sigma}}{\partial a_\sigma} \delta a_\sigma = 0 \tag{56}$$

Rewriting this equation yields

$$\delta a_\sigma = \underbrace{ - \left[\frac{\partial R_{a_\sigma}}{\partial a_\sigma} \right]^{-1} \frac{\partial R_{a_\sigma}}{\partial \mathbf{F}} }_{\frac{\partial a}{\partial \mathbf{F}}} : \delta \mathbf{F} \tag{57}$$

where the derivative $\partial a/\partial \mathbf{F}$ is identified. Note that $\partial R_{a_\sigma}/\partial a_\sigma$ is the Jacobian of the *external* scheme (Eq. (49)). The second term is given in Appendix C.

Remark 6. In total, $2N + 1$ *consistency conditions* are used to derive the tangent modulus.

3. Parameter identification

To determine the (single-mode) yield parameters of the mesoscopic constitutive model, we consider a material point under uniaxial tension

and compression with off-axis angle θ_0 at constant strain rate $\dot{\varepsilon}$ (see Fig. 6). In addition, we assume small deformations at the moment of yielding, such that: $\hat{a} = a_0$, $\sigma = \Sigma = \Sigma^{\text{sym}}$, and $\bar{\sigma} = \bar{\Sigma}$. Furthermore, we choose an orthonormal basis $\{e_i\}_{i=1,2,3}$ where unit vector e_1 is aligned with the load direction. The flow rule (Eq. (8)) gives the rate of plastic deformation in the load direction

$$D_{11}^{\text{p}} = \frac{\sigma_0}{\eta_0} \sinh \left(\frac{\bar{\sigma}}{\sigma_0} \right) \exp \left(-\mu_{\text{p}} \frac{I_3}{\sigma_0} \right) \frac{\partial \bar{\sigma}}{\partial \sigma_{11}} \tag{58}$$

Plastic and elastic deformations develop simultaneously until the rate of plastic deformation is equal to the applied strain rate ($D_{11}^{\text{p}} = \dot{\varepsilon}$) upon which the stress reaches a plateau,[4] which marks the moment of yielding. When the material yields, $\bar{\sigma} \gg \sigma_0$ and the hyperbolic sine function can be approximated with an exponential function

$$\dot{\varepsilon} \approx \frac{\sigma_0}{2\eta_0} \exp \left(\frac{\bar{\sigma} - \mu_{\text{p}} I_3}{\sigma_0} \right) \frac{\partial \bar{\sigma}}{\partial \sigma_{11}} \tag{59}$$

This equation provides an analytical relation between the applied strain rate $\dot{\varepsilon}$ and the equivalent stress $\bar{\sigma}$ at the moment of yielding.

3.1. Transverse tension and compression

The parameters μ_{p}, σ_0 and η_0 can be determined from stress–strain curves of uniaxial tension and compression under off-axis angle $\theta_0 = 90°$ at equal strain rates. For this angle, I_2 is zero and α_2 is eliminated from the equations. The transversely isotropic stress invariants at the moment of yielding read

$$I_1 = \frac{\sigma_{\text{y},90}^2}{4}, \quad I_2 = 0, \quad I_3 = \begin{cases} \sigma_{\text{y},90\text{t}} & \text{in tension} \\ -\sigma_{\text{y},90\text{c}} & \text{in compression} \end{cases} \tag{60}$$

where $\sigma_{\text{y},90}$ is the yield stress at $\theta = 90°$. Substitution in Eq. (23) and (30) and rewriting Eqs. (59) provides the following expressions of the yield stresses in tension $\sigma_{\text{y},90\text{t}}$ and compression $\sigma_{\text{y},90\text{c}}$

$$\sigma_{\text{y},90\text{t}} = \frac{\sigma_0}{\frac{1}{\sqrt{2}} + \mu_{\text{p}}} \ln \left(2\sqrt{2} \frac{\eta_0}{\sigma_0} \dot{\varepsilon} \right) \tag{61}$$

$$\sigma_{\text{y},90\text{c}} = \frac{\sigma_0}{\frac{1}{\sqrt{2}} - \mu_{\text{p}}} \ln \left(2\sqrt{2} \frac{\eta_0}{\sigma_0} |\dot{\varepsilon}| \right) \tag{62}$$

When the yield stresses $\sigma_{\text{y},90\text{t}}$ and $\sigma_{\text{y},90\text{c}}$ are known, μ_{p} is solved for, which gives the following closed-form relation

$$\mu_{\text{p}} = \frac{1}{\sqrt{2}} \left(\frac{\sigma_{\text{y},90\text{c}} - \sigma_{\text{y},90t}}{\sigma_{\text{y},90\text{c}} + \sigma_{\text{y},90t}} \right) \tag{63}$$

With μ_{p} known, σ_0 and η_0 are determined from an Eyring plot for uniaxial compression. This requires at least two compression curves at different strain rates. Eq. (62) is rearranged as

$$\sigma_{\text{y},90\text{c}} = \underbrace{ \frac{\sigma_0 \ln(10)}{\frac{1}{\sqrt{2}} - \mu_{\text{p}}} }_{\text{slope } m} \left[\log_{10}(|\dot{\varepsilon}|) + \log_{10} \left(2\sqrt{2} \frac{\eta_0}{\sigma_0} \right) \right] \tag{64}$$

---

[4] Under large deformations, a geometric hardening or softening response may occur due to re-orientation of the fibers.

Table 1
Overview of all model parameters and required tests.

Parameters	Names	Tests	Identification method
$E_{11}, E_{22}, G_{12}, \nu_{21}$	Elastic constants	Basic tests to identify elastic properties	–
μ_p	Pressure parameter	Transverse tension and compression tests[a]	Eq. (63)
η_0, σ_0	Eyring parameters	Two transverse tests[b]	Eqs. (65) and (66)
α_2	Anisotropy parameter	Single off-axis test under tension or compression	Eq. (67)
$\{m_i\}_{i=1}^N, \{\eta_{0i}\}_{i=1}^N$	Relaxation spectrum	Single off-axis test under tension or compression	Procedure in Section 2.5

[a] Same strain rate.

[b] At least two different strain rates.

where m is the slope in a semi-log plot of yield stress $\sigma_{y,90c}$ *vs* strain rate $\dot{\varepsilon}$. From the slope, σ_0 and η_0 are given by

$$\sigma_0 = m \left(\frac{\frac{1}{\sqrt{2}} - \mu_p}{\ln(10)} \right) \tag{65}$$

$$\eta_0 = \frac{\sigma_0 \, 10^{\frac{\sigma_{y,90c}}{m}}}{2\sqrt{2}\,\dot{\varepsilon}} \tag{66}$$

3.2. Off-axis loading in tension

Parameter α_2 can be obtained from any other test where I_2 is non-zero, for example the $\theta_0 = 30°$ case. By following the same steps as before, the analytical yield stress for this angle reads

$$\sigma_{y,30t} = \frac{4\sigma_0}{\mu_p + \sqrt{\frac{1}{2} + 6\alpha_2}} \ln \left(\frac{8}{\sqrt{\frac{1}{2} + 6\alpha_2}} \frac{\eta_0}{\sigma_0} \dot{\varepsilon} \right) \tag{67}$$

which is a nonlinear equation in its argument α_2 that can be solved numerically, given $\eta_0, \sigma_0, \mu_p, \sigma_{y,30t}$ and corresponding strain rate $\dot{\varepsilon}$.

3.3. Summary of model parameters

The parameters of the mesomodel are determined in the next section with a micromodel for carbon/PEEK under uniaxial off-axis strain rates. Alternatively, experimental off-axis coupon tests with oblique ends may be used Sun and Chung (1993). An overview of all model parameters, the required tests to obtain their values and the corresponding formulas presented in this section, is given in Table 1.

4. Numerical homogenization of a micromodel

The parameters of the mesoscopic material model are determined by homogenizing a previously calibrated micromodel, with periodic boundary conditions, for carbon/PEEK (Kovačević et al., 2022). The micromodel comprises of hyperelastic transversely isotropic fibers and viscoplastic polymer matrix, where the latter is modeled with the original isotropic EGP model (Tervoort et al., 1996; Van Breemen et al., 2011). The micromodel and mesomodel are schematically depicted in Fig. 7.

4.1. Boundary conditions for off-axis loading

Applying off-axis loads to the micromodel (as shown in Fig. 6) is not straightforward. Since periodic boundary conditions are applied, it is not possible to vary the fiber angle inside the micromodel, which would violate the assumption of continuous fibers as imposed by the periodicity. Instead, off-axis loading is achieved by aligning the micromodel with the fibers, while a global deformation is applied in the local frame of the micromodel. Since the local frame changes under off-axis loading due to re-orientation of the fibers (see Fig. 6), a special constraint equation is used that accounts for these re-orientations (Kovačević and van der Meer, 2022; Kovačević et al., 2024).

In contrast, global deformations can straightforwardly be applied on a single element with the mesoscopic model. Off-axis loading is then

Table 2
Elasticity constants.

E_1 [GPa]	E_2 [GPa]	G_{12} [GPa]	ν_{21}
55.5	7.4	4.8	0.016

Table 3
Plasticity parameters.

μ_p	σ_0 [MPa]	η_0 [MPa s]	α_2
0.053	1.71	5.90×10^{29}	1.147

Table 4
Relaxation spectrum.

Mode i	m_i [–]	η_{0i} [MPa s]	Mode i	m_i [–]	η_{0i} [MPa s]
1	0.020	1.002×10^6	13	0.014	2.453×10^{24}
2	0.033	1.486×10^9	14	0.023	1.131×10^{25}
3	0.040	1.025×10^{12}	15	0.014	1.654×10^{25}
4	0.053	1.963×10^{14}	16	0.016	3.367×10^{25}
5	0.051	2.726×10^{16}	17	0.018	7.969×10^{25}
6	0.054	1.089×10^{18}	18	0.021	1.920×10^{26}
7	0.056	6.664×10^{19}	19	0.006	9.983×10^{25}
8	0.034	3.867×10^{20}	20	0.029	7.309×10^{26}
9	0.037	6.447×10^{21}	21	0.052	4.257×10^{27}
10	0.031	4.479×10^{22}	22	0.011	1.396×10^{27}
11	0.034	2.799×10^{23}	23	0.029	6.464×10^{27}
12	0.032	2.048×10^{24}	24	0.292	5.920×10^{29}

achieved by varying the initial fiber direction vector a_0, while applying the load in the e_1-direction. Although the methods to apply boundary conditions on the micromodel and the mesomodel are different, the resulting (global) deformations are the same.

4.2. Elasticity parameters

The elasticity parameters of the mesoscopic material model are determined by subjecting the micromodel to three basic load cases: longitudinal tension, longitudinal shear and transverse shear. The transversely isotropic elasticity constants are given in Table 2.

4.3. Plasticity parameters

The mesoscopic yield parameters are obtained with the analytical expressions derived in Section 3. To obtain the pressure-dependency parameter μ_p, the micromodel is subjected to uniaxial transverse compression and tension under true strain rate $\dot{\varepsilon} = 10^{-3}\,\text{s}^{-1}$. For finding η_0 and σ_0, the micromodel is subjected to three strain rates under transverse compression. The stress–strain curves are shown in Fig. 8. Note that these curves do not reach a plateau due to hardening, which obscures a clear yield point. In this work, the point at which the stress starts to increase almost linearly is chosen as the 'yield' stress. The resulting mesoscopic parameters are tabulated in Table 3. The fit of the Eyring curve (Eq. (64)) with the transverse compression yield data is shown in Fig. 9.

The micromodel is subjected to uniaxial tension under off-axis angle $\theta_0 = 30°$ and true strain rate $\dot{\varepsilon} = 10^{-3}\,\text{s}^{-1}$. The parameter α_2 is first determined by solving Eq. (67). With all single-mode parameters
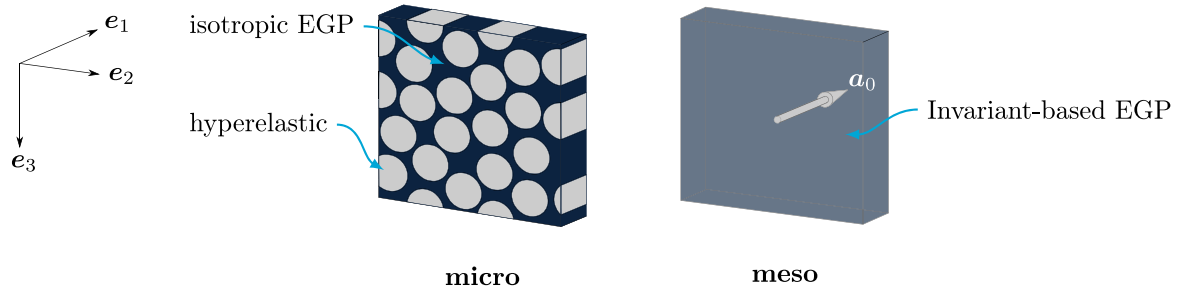
Fig. 7. Micromodel with hyperelastic fibers and isotropic EGP model for the matrix *vs* mesomodel with proposed invariant-based EGP model and fiber direction vector $\boldsymbol{a}_0$.
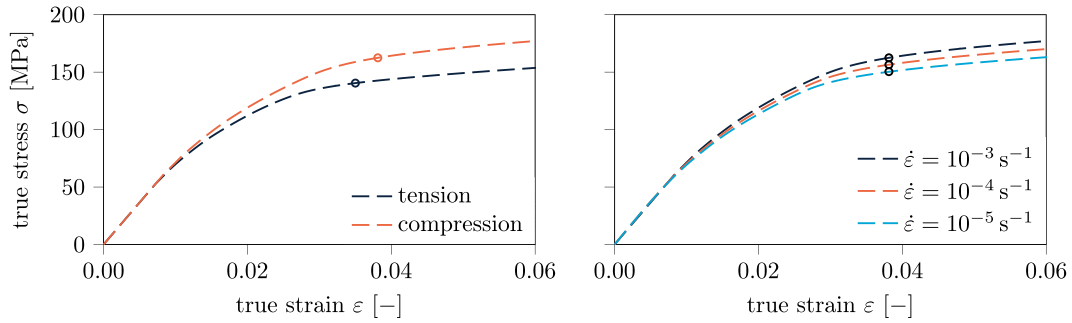

Fig. 8. Input curves generated with micromodel at $\theta_0 = 90°$: (*left*) transverse tension and compression under strain rate $\dot{\varepsilon} = 10^{-3}\,\mathrm{s}^{-1}$ and (*right*) transverse compression under three different strain rates. The yield stresses are indicated with a dot.
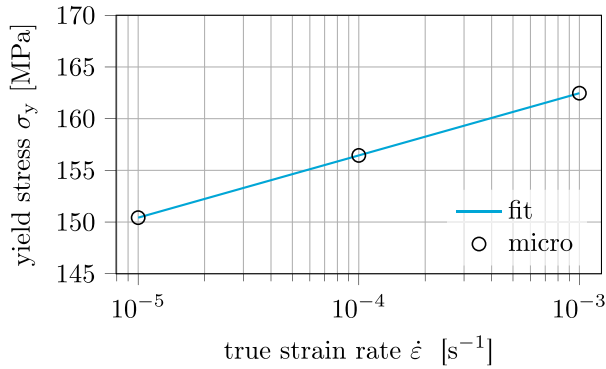

Fig. 9. Eyring fit (Eq. (64)) of yield stress versus strain rate for $\theta_0 = 90°$ in compression.
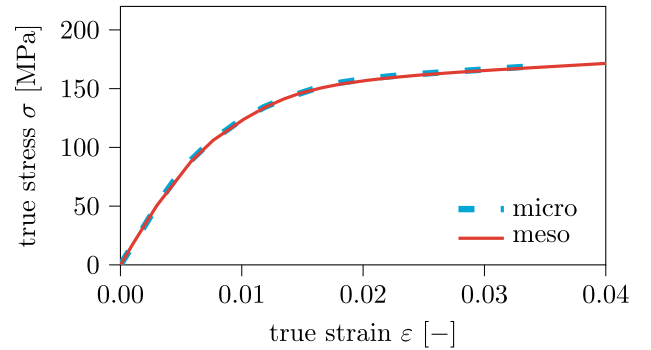
Fig. 10. Multimode calibration with uniaxial tension under $\theta_0 = 30°$ and $\dot{\varepsilon} = 10^{-3}\,\mathrm{s}^{-1}$: output curve with mesomodel (*meso*) *vs* input curve with micromodel (*micro*).

known, a multimode relaxation spectrum, with 24 modes is determined by following the procedure as outlined in Section 2.5. This number of modes follows from the recommendation in Ref. Amiri-Rad et al. (2019) and Van Breemen et al. (2011), to include one mode per decade in the relaxation spectrum, ensuring an accurate pre-yield and creep response. A smaller number of modes may introduce spurious oscillations in the stress–strain curve (Van Breemen et al., 2011).

Applying the method by Refs. Van Breemen et al. (2011) and Amiri-Rad et al. (2019) (as outlined in Section 2.5) to the present mesoscopic model, resulted in a slight mismatch between the input and output results. Therefore, the input curve is iteratively adjusted such that the output curve matched with the original input curve. The relaxation spectrum is tabulated in Table 4. With the ratios $\{m_i\}$, the elasticity parameters are obtained for each mode with Eq. (41) and Table 2. The resulting stress–strain curve is shown in Fig. 10.

Remark 7. Other invariant-based (Perzyna-type) viscoplasticity models (Koerber et al., 2018; Gerbaud et al., 2019; Rodrigues Lopes et al., 2022), more suitable for unidirectional *thermosetting* polymer composites, require six hardening functions as inputs (obtained from bi-axial tension/compression, longitudinal shear, transverse shear and uniaxial tension/compression tests) to describe the nonlinear rate-dependent plastic response. However, obtaining transverse shear and biaxial test data through experiments is not straightforward. Therefore, these hardening functions are usually deduced from other tests, engineering assumptions or micromechanical models (Vogler et al., 2013). With the present invariant-based non-Newtonian flow model for *thermoplastic* polymer composites, the yield stress is determined by the mode with the highest initial viscosity (see Fig. 4), and thus, only four parameters are required. These parameters can be determined from a small number of off-axis constant strain-rate tests as shown in this section with a micromodel, or from off-axis coupon tests with oblique ends under
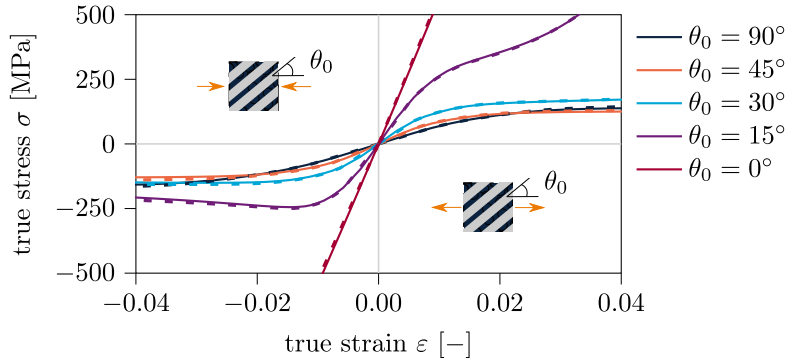
Fig. 11. Stress–strain curves under various initial off-axis angles θ_0 and constant strain rate $\dot{\varepsilon} = 10^{-3}\,\text{s}^{-1}$ in tension and compression: micromodel (*dashed* line) *vs* mesomodel (*solid* line).

(almost) uniform stress states (Sun and Chung, 1993). Subsequently, the pre-yield nonlinearity is described by a relaxation spectrum, which can be determined from a *single* stress–strain curve under off-axis loading. Therefore, a significant reduction in the amount of necessary inputs is achieved with the present invariant-based constitutive model.

5. Results

The material parameters of the mesomodel are determined in the previous section through calibration against a micromodel for carbon/PEEK (Kovačević et al., 2022). For this purpose, no more than five stress–strain curves were used. The performance of the mesoscopic constitutive model in simulating rate-dependent plasticity and creep is studied in this section. First, its capability in representing a material point of a composite under various off-axis angles, strain-rates and creep loads is assessed with a single element, under the assumption of a uniform deformation (see Fig. 6). Subsequently, the model is applied to the simulation of ply-level off-axis specimens and compared against experiments (Sundararajan, 2024).

5.1. Constant strain rate

The microscale and mesoscale model are subjected to constant true strain rates $\dot{\varepsilon}\,(\text{s}^{-1}) \in \{10^{-5}, 10^{-4}, 10^{-3}\}$ under off-axis angles $\theta\,(°) \in \{90, 45, 30, 15, 0\}$ in tension and compression.

Direction-dependence Fig. 11 shows the stress–strain curves with $\dot{\varepsilon} = 10^{-3}\,\text{s}^{-1}$ and various off-axis angles θ_0. It is observed that the strongly anisotropic response of the micromodel is well represented with the mesoscale model: under $\theta_0 = 0°$, the response is elastic, whereas under off-axis loading, it is viscoplastic. It is worth noting that the rather simple approach, as described in Section 2.5, of finding a relaxation spectrum with a single stress–strain curve, gives a good pre-yield response for all off-axis angles and strain rates.

With both the micromodel and the mesomodel under off-axis angle $\theta_0 = 15°$ in tension, an increasing stiffness (hardening) is observed in the post-yield regime, whereas under compression, a softening response is obtained. When off-axis tensile loads are applied to the composite material, the fibers progressively align with the load direction (see Fig. 6). This re-orientation of the fibers is captured by the mesoscale model and is numerically depicted in Fig. 12. In contrast, under compression, the opposite effect takes place where the off-axis angle increases, leading to a softening response. The agreement between the two models indicates that the re-orientation of the fibers is captured just as well in the mesoscopic constitutive model as in the micromodel where the fibers are explicitly modeled.
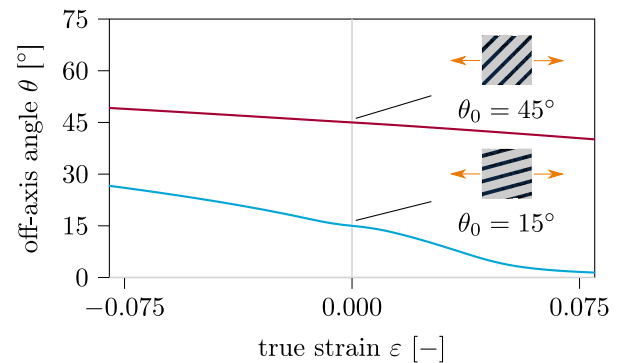

Fig. 12. Evolution of the off-axis angle θ with the mesoscale model for two *initial* off-axis angles $\theta_0\,(°) \in \{15, 30\}$.

Rate-dependence The stress–strain curves with off-axis angles $\theta_0\,(°) \in \{15, 30, 45, 90\}$ and constant strain rates $\dot{\varepsilon}\,(\text{s}^{-1}) \in \{10^{-5}, 10^{-4}, 10^{-3}\}$ in tension are shown in Fig. 13. It can be observed that the rate-dependence, which describes an increasing yield stress with increasing strain rate, is accurately reflected by the mesoscale model. The yield stresses from the mesoscale model are indicated in Fig. 13 and plotted against strain rates $\dot{\varepsilon}$ on a double logarithmic scale for each off-axis angle θ_0 in Fig. 14. In line with experimental observations for unidirectional polymer composites (Erartsin et al., 2022), the curves are parallel, indicating a factorizable dependence of yield stress on strain rate $\dot{\varepsilon}$ and off-axis angle θ_0.

Pressure-dependence The stress–strain curves of the micromodel and the mesomodel under transverse tension and compression with $\dot{\varepsilon} = 10^{-3}\,\text{s}^{-1}$ are shown in Fig. 15. It can be observed that the response is accurate until the yield point. However, after yielding, a hardening response is observed with the micromodel. In the isotropic EGP for the matrix material of the micromodel, an (elastic) hardening contribution is present (Kovačević et al., 2024), representing polymer chain re-orientation, which is currently not included in the mesoscale model. In contrast, under off-axis loading, the post-yield hardening response is captured by the mesoscale model (see Fig. 13). This type of hardening is due to re-orientation of fibers and is of geometric nature (see Figs. 6 and 12). Under pure transverse loading, re-orientation of the fibers does not occur while polymer chain re-orientation of the matrix does take place.

Under transverse tensile loading, Carbon/PEEK fractures before a fully developed plastic response is reached due to large hydrostatic stresses in the polymer matrix. The post-yield hardening response is
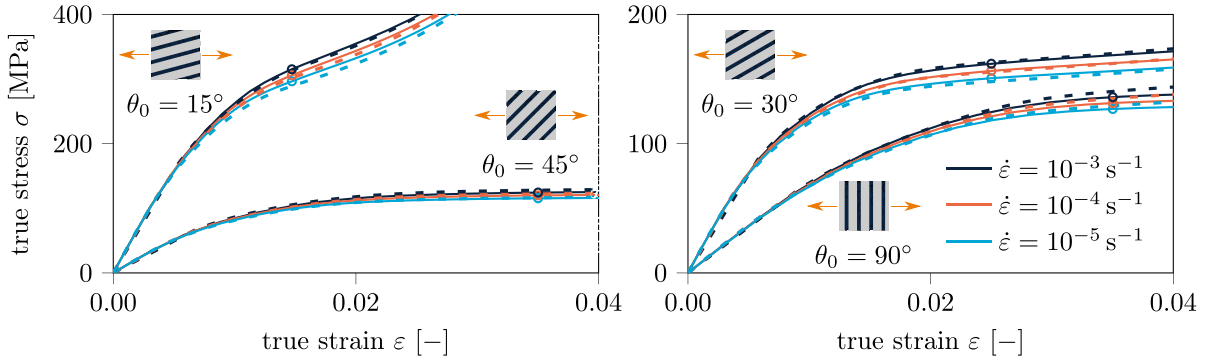
Fig. 13. Rate-dependence under uniaxial tension with various initial off-axis angles θ_0 and strain rates $\dot{\varepsilon}$: micromodel (*dashed* line) vs. mesomodel (*solid* line). The yield stresses are indicated with a dot.
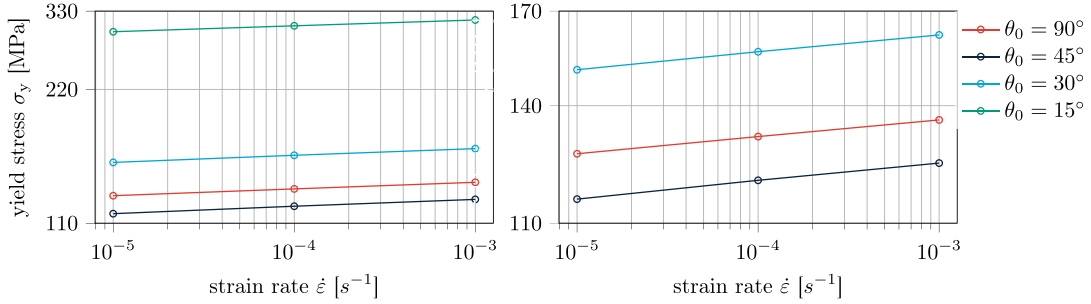

Fig. 14. Yield stress as function of strain rate for various off-axis angles θ_0 with mesoscale model. The figure on the left contains the curves of all off-axis angles, whereas the figure on the right omits the curve for $\theta_0 = 15°$ to show the rate-dependence on a smaller range of y-axis values.
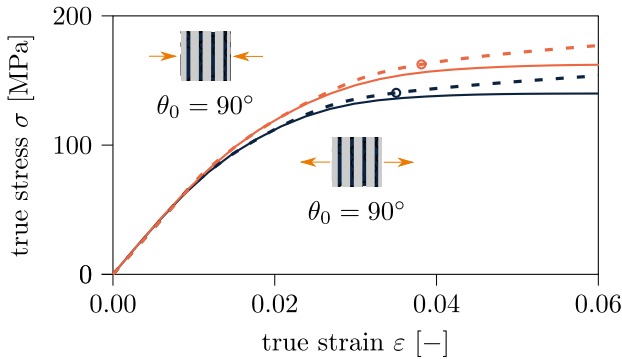
Fig. 15. Transverse tension and compression under off-axis angle $\theta_0 = 90°$: micromodel (*dashed* line) with yield stresses (indicated with a dot) vs. meso-model (*solid* line).
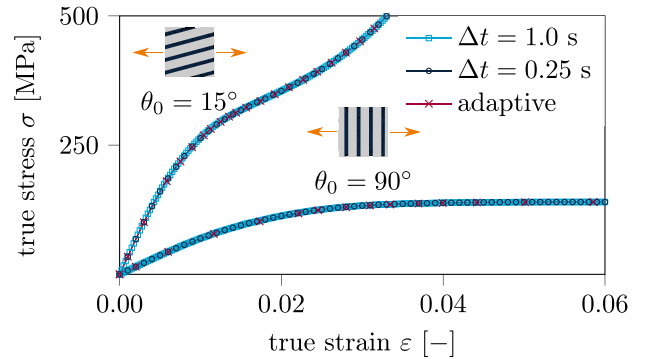
Fig. 16. Time-step dependence: stress–strain curves with two different fixed time-steps and adaptive steps. The markers denote the time-steps.

therefore less relevant under tensile loading. However, for a more accurate post-yield response under transverse compression, an (anisotropic) hardening contribution can be included to account for this effect.

Time-step dependence The time-step dependence of the time integration scheme, with the Padé approximation (Eq. (45)), is assessed by comparing the response obtained with adaptive stepping based on global iterations (Hofman et al., 2024), to the response with fixed time increments. For this purpose, simulations with off-axis constant strain rates $\dot{\varepsilon} = 10^{-3}\,\text{s}^{-1}$ under $\theta_0 = 15°$ and $90°$ are used for the comparison. The simulations with fixed time steps are performed with $\Delta t = 1.0\,\text{s}$ and $0.25\,\text{s}$, resulting in strain increments $\Delta\varepsilon = 10^{-3}$ and 2.5×10^{-4}, respectively. Fig. 16 shows the stress–strain curves, from which it is concluded that time-step dependence of the time integration scheme is negligible. In combination with the fully consistent tangent stiffness, adaptive stepping based on global iterations is possible for efficient simulations with high accuracy.

5.2. Creep

An important feature of the EGP model is the capability to simulate not only rate-dependent plasticity but also creep in polymers. This also holds for the present mesoscopic version for polymer composites. To assess the performance under creep, the micro- and meso-scale models are subjected to a constant tensile *engineering* stress rate until a specified stress level is reached in $10\,\text{s}$. After this phase, the engineering stress is kept constant.

The engineering strain as a function of time is shown in Fig. 17 for four off-axis angles $\theta\,(°) \in \{90, 45, 30, 15\}$. For each angle, three different engineering stress levels are applied, as indicated in the figures. It can be observed that for all off-axis angles, the strains of the mesomodel during the ramp-up to the maximum engineering stress are in close agreement with those of the micromodel. This is expected since the mesoscale model parameters were determined with (short-term) constant-strain rate data (Section 4). After reaching the
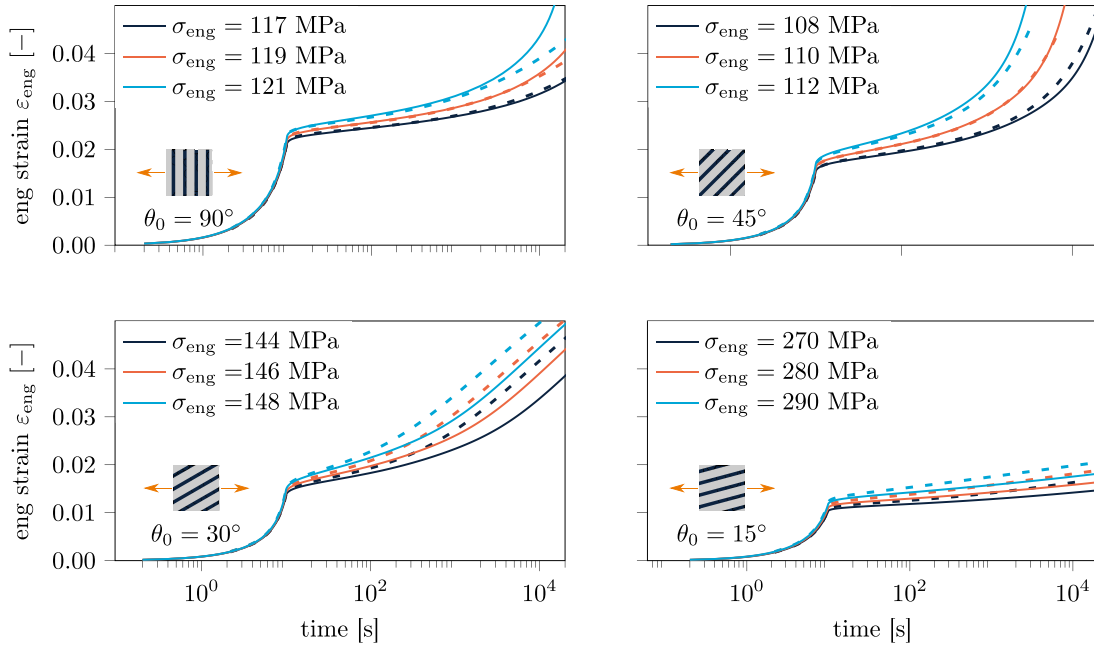
Fig. 17. Creep response under various off-axis angles θ_0 and engineering stress levels σ_{eng}: micromodel (*dashed* line) vs. mesomodel (*solid* line).
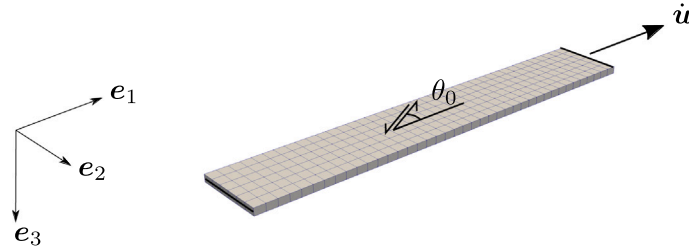

Fig. 18. Ply simulation: mesh and initial off-axis angle θ_0 of the fiber with respect to the load.

maximum applied stress level, the creep response with $\theta_0 = 45°$ is very similar to that of the micromodel. However, for the other angles, the match is adequate but not as good as with $\theta_0 = 45°$. It is somewhat surprising that, although the $\theta_0 = 30°$ off-axis angle has been used for determining the multi-mode relaxation spectrum (see Fig. 10), the match in creep is worse than with the other off-axis angles. A parameter identification procedure which includes creep data, *e.g.* through a compliance-time master curve from a series of creep tests at different stress levels (Tervoort et al., 1996), may improve the creep response.

5.3. Unidirectional ply under off-axis tensile loading

So far, material point analyses have been carried out with the mesoscale model. In this section, the mesoscale model is used for the simulation of a unidirectional ply with dimensions 120×15×1.8 mm. The three-dimensional mesh, consisting of 240 trilinear finite elements, is shown in Fig. 18. On each end of the specimen, the displacements in the e_2- and e_3-direction are fixed, mimicking the constraining effect of the grips in the experimental test (Sundararajan, 2024). In the e_1-direction, a constant *engineering* strain rate of $\dot{\varepsilon}_{\text{eng}} = 10^{-4}\,\text{s}^{-1}$ is enforced. This is achieved by applying a displacement rate $\dot{u} = 120\,\dot{\varepsilon}_{\text{eng}}$ at one end, while at the other end, the displacement is fixed. The engineering stress σ_{eng} is computed from the resulting force in e_1-direction, divided by the undeformed area of the surface at the end. Simulations are performed with four initial off-axis angles $\theta_0\,(°) \in \{15, 30, 45, 90\}$.

The engineering stress–strain curves are shown in Fig. 19. The ply simulations give an excellent match with the experiments for $\theta_0 = 30°$,

45° and 90°. For $\theta_0 = 15°$, although the pre-yield stiffness is slightly over-predicted and the post-yield hardening response is slightly under-predicted, the overall agreement is satisfactory. It has been observed in Section 5.1 that the mesomodel and micromodel under uniform tension with $\theta_0 = 15°$ showed a pronounced upswing of the stress after yielding (see Fig. 11), due to an increasing alignment of the fibers with the load direction. The same type of re-orientation is prevented by the grips in the coupon test and this constraining effect is captured by simulating the ply with the mesomodel. This can be illustrated by plotting the evolution of off-axis angle (θ) and plastic deformation component in e_1-direction (F_{11}^p), for the mode with the highest initial viscosity (mode 24 in Table 4), at three different time-steps (see Fig. 20). As the fibers tend to align with the load direction near the ends $(\theta < \theta_0)$, the off-axis angles increase in the middle of the specimen $(\theta > \theta_0)$, which is opposite to the direction of re-orientation as was previously seen with the single element test under tension (see Fig. 12). This increase of matrix-dominated loading, combined with the presence of stress concentrations in the ply specimen, results in an earlier development of plasticity with respect to the single element and a better match with the experiments (see Fig. 20, *top*).

The deformations in the coupon test are inhomogeneous and cannot be used directly as material input. To obtain a more homogeneous deformation state, off-axis specimens with oblique tabs may be used (Sun and Chung, 1993). The analytical parameter identification procedure outlined in Section 3 may then be directly applied to experimental data of off-axis constant strain rates, without requiring a pre-calibrated micromodel to generate inputs for the mesoscopic constitutive model.
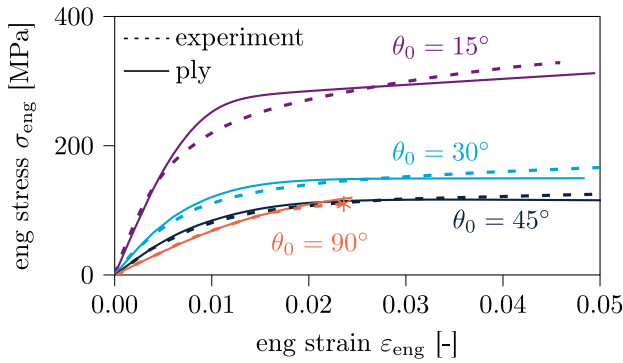
Fig. 19. Ply simulations *vs.* experiments with θ_0 (°) = {15, 30, 45, 90}. The experiment with $\theta_0 = 90°$ fractured (indicated with ∗) before plasticity fully developed.

6. Conclusion

A mesoscopic constitutive model for simulating rate-dependent plasticity and creep in unidirectional thermoplastic composites has been presented. The model is an extension of a viscoplastic material model for isotropic polymers with an Eyring-type non-Newtonian flow rule. Strong anisotropy is incorporated through the use of three transversely isotropic stress invariants in the flow rule. As a result, plastic flow in fiber direction is removed and pressure-dependency of the polymer matrix is taken into account by extending the Eyring relation with anisotropic pressure dependence. An important feature of the present invariant-based anisotropic viscoplasticity model is that it can describe both rate-dependent plasticity and creep in thermoplastic polymer composites with non-Newtonian flow.

The constitutive equations are implicitly integrated, which allows for the use of relatively large time steps. Furthermore, a consistent tangent stiffness modulus has been derived by linearizing the stress update algorithm. The model requires four viscoplasticity-related input parameters to describe direction-, rate- and pressure-dependent plasticity and creep, obtained from a few stress–strain curves under off-axis loading. For an accurate pre-yield and creep response, multiple modes can be used with a relaxation spectrum determined from a *single* stress–strain curve. In this manuscript, a micromodel for unidirectional carbon/PEEK is used to determine the mesoscale model parameters. However, off-axis coupon tests with oblique ends may also be used.

The mesoscopic constitutive model has been compared to a previously developed micromodel for unidirectional carbon/PEEK. It has been shown that the mesoscale model gives a response similar to the micromodel under various strain rates and off-axis angles. However, under transverse compression, a hardening contribution can be included for an improved post-yield response. The model gives satisfactory results under creep, although not as good as under constant strain rates. This may indicate that the parameter identification procedure, solely based on (short-term) constant strain rate data, requires further improvements.

Finally, the mesoscale model has been applied to the simulation of unidirectional composite coupon tests under off-axis strain rates and shows a good agreement with experiments. The development of the mesoscopic constitutive model, with a few model parameters, while retaining a high degree of the accuracy of a detailed micromodel, is an important step towards virtual testing of thermoplastic composite laminates. Further extensions can be made to cover multiple relaxation processes and to include temperature dependence.

Summary of contributions The EGP model has been extended for unidirectional thermoplastic composites. Compared to other anisotropic versions of the EGP model for *short* and *long* fiber composites (Amiri-Rad et al., 2019; Amiri-Rad et al., 2021), new features of the present model are:

- Strong anisotropy is described by transversely isotropic stress invariants
- Plastic flow in fiber direction is removed
- The Eyring-type viscosity function is extended with anisotropic pressure dependence
- The constitutive equations are implicitly integrated and consistently linearized
- The model is formulated in global frame and does not require rotations to local frame

Compared to previous invariant-based Perzyna-type viscoplasticity models for unidirectional composites (Koerber et al., 2018; Gerbaud et al., 2019; Rodrigues Lopes et al., 2022):

- An Eyring-type non-Newtonian flow rule, suitable for *thermoplastic* composites, is used to describe both rate-dependent plasticity and creep
- Only four parameters and a relaxation spectrum are required, which can be obtained from a small number of off-axis tests (either with a micromodel or with off-axis coupon tests with oblique ends)
- The present anisotropic model allows for future extensions regarding the effects of aging (Klompen et al., 2005), temperature dependence (Tervoort et al., 1998) and to cover multiple relaxation processes (Klompen and Govaert, 1999) through the Eyring relation

CRediT authorship contribution statement

P. Hofman: Writing – original draft, Visualization, Validation, Software, Methodology, Conceptualization. **D. Kovačević:** Writing – review & editing, Software. **F.P. van der Meer:** Writing – review & editing, Supervision, Funding acquisition. **L.J. Sluys:** Writing – review & editing, Supervision, Funding acquisition.

Declaration of competing interest

The authors declare that they have no known competing financial interests or personal relationships that could have appeared to influence the work reported in this paper.

Acknowledgment

Appendix A. Jacobian internal Newton–Raphson scheme

The Jacobian for solving the plastic deformation gradient $\mathbf{F}_{\mathrm{p}i}$ with the internal scheme of each mode i is determined in this appendix. To improve readability, subscript i is dropped and index notation is used. The residual for *each* mode reads

$$R_{ij}^{\mathbf{F}_{\mathrm{p}i}} = F_{ij}^{\mathrm{p}} - f_{ij} \tag{A.1}$$

where

$$f_{ij} = \Pi_{ik} F_{kj}^{\mathrm{p},0} \tag{A.2}$$

with

$$\Pi_{ik} = \left(\underbrace{\delta_{il} - \frac{\Delta t}{2} \hat{D}_{il}^{\mathrm{p}}}_{Z_{il}} \right)^{-1} \left(\underbrace{\delta_{lk} + \frac{\Delta t}{2} \hat{D}_{lk}^{\mathrm{p}}}_{Y_{lk}} \right) \tag{A.3}$$
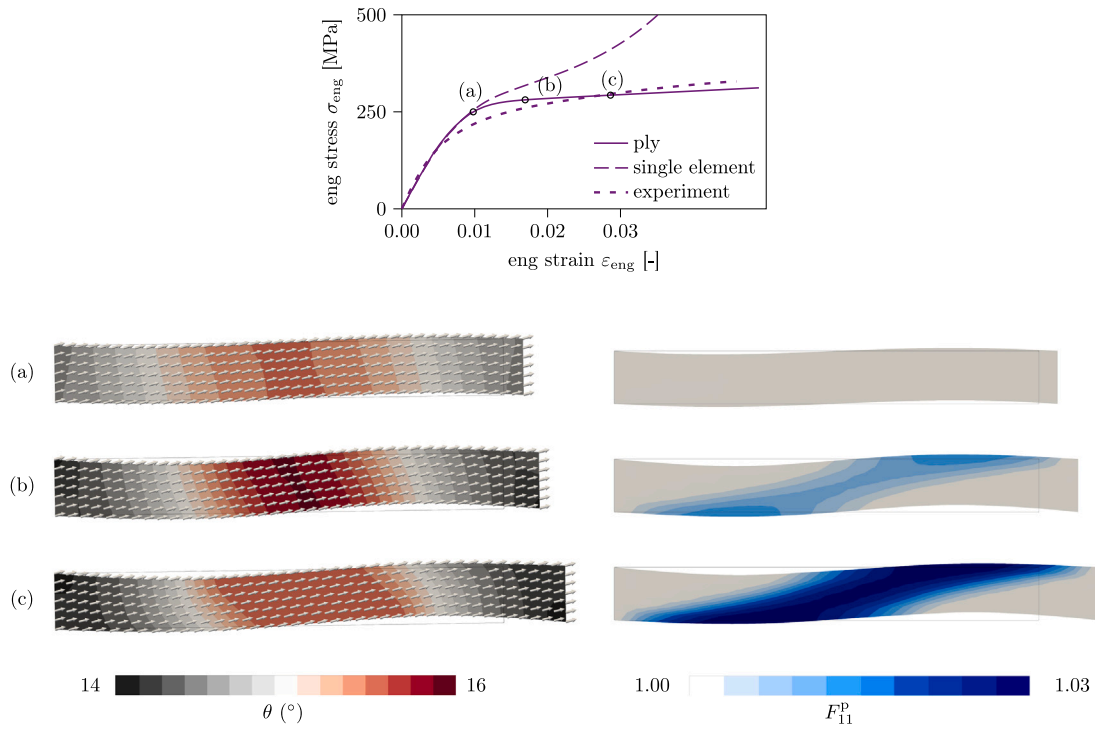
Fig. 20. Ply simulation with $\theta_0 = 15°$: evolution of fiber angle θ (*left*) and plastic deformation F_{11}^{p} in load direction for the mode with highest initial viscosity (*right*) at indicated time instances on the stress–strain plot (*top*). For comparison, the response of a single element test with $\dot{\varepsilon}_{\mathrm{eng}} = 10^{-4}\,\mathrm{s}^{-1}$ and the experimental curve are added to the stress–strain diagram. Deformed mesh is magnified (×5).

Taking the derivative of Eq. (A.1) with respect to the plastic deformation gradient gives the Jacobian

$$\frac{\partial R_{ij}^{\mathbf{F}_{pi}}}{\partial F_{mn}^{\mathrm{p}}} = \delta_{im}\delta_{jn} - \frac{\partial f_{ij}}{\partial \Pi_{kl}}\frac{\partial \Pi_{kl}}{\partial \hat{D}_{uv}^{\mathrm{p}}}\left[\frac{\partial \hat{D}_{uv}^{\mathrm{p}}}{\partial \Sigma_{qp}^{\mathrm{sym}}}\frac{\partial \Sigma_{qp}^{\mathrm{sym}}}{\partial F_{rs}^{\mathrm{e}}}\frac{\partial F_{rs}^{\mathrm{e}}}{\partial F_{mn}^{\mathrm{p}}} + \frac{\partial \hat{D}_{uv}^{\mathrm{p}}}{\partial \hat{a}_{w}}\frac{\partial \hat{a}_{w}}{\partial F_{mn}^{\mathrm{p}}}\right] \quad (A.4)$$

where

$$\frac{\partial f_{ij}}{\partial \Pi_{mn}} = \delta_{im}F_{nj}^{\mathrm{p},0} \quad (A.5)$$

$$\frac{\partial \Pi_{ij}}{\partial \hat{D}_{mn}^{\mathrm{p}}} = \frac{\partial Z_{ik}^{-1}}{\partial \hat{D}_{mn}^{\mathrm{p}}}Y_{kj} + Z_{ik}\frac{\partial Y_{kj}}{\partial \hat{D}_{mn}^{\mathrm{p}}} \quad (A.6)$$

with

$$\frac{\partial Z_{kj}^{-1}}{\partial \hat{D}_{mn}^{\mathrm{p}}} = -Z_{ik}^{-1}\frac{\partial Z_{ir}}{\partial \hat{D}_{mn}^{\mathrm{p}}}Z_{rj}^{-1} \quad (A.7)$$

$$\frac{\partial Z_{ij}}{\partial \hat{D}_{mn}^{\mathrm{p}}} = -\frac{\Delta t}{2}\delta_{im}\delta_{jn} \quad (A.8)$$

$$\frac{\partial Y_{ij}}{\partial \hat{D}_{mn}^{\mathrm{p}}} = \frac{\Delta t}{2}\delta_{im}\delta_{jn} \quad (A.9)$$

The other derivatives read

$$\frac{\partial \hat{D}_{ij}^{\mathrm{p}}}{\partial \Sigma_{mn}^{\mathrm{sym}}} = \frac{1}{\eta}\left[\hat{N}_{mn}^{\mathrm{p}}\hat{N}_{ij}^{\mathrm{p}} + \bar{\Sigma}\frac{\partial \hat{N}_{ij}^{\mathrm{p}}}{\partial \Sigma_{mn}^{\mathrm{sym}}}\right] \quad (A.10)$$

$$\frac{\partial \Sigma_{ij}^{\mathrm{sym}}}{\partial F_{mn}^{\mathrm{e}}} = \frac{1}{2}\left(\frac{\partial \Sigma_{ij}}{\partial F_{mn}^{\mathrm{e}}} + \frac{\partial \Sigma_{ji}}{\partial F_{mn}^{\mathrm{e}}}\right) \quad (A.11)$$

$$\frac{\partial F_{rs}^{\mathrm{e}}}{\partial F_{mn}^{\mathrm{p}}} = -F_{rk}\left(F_{km}^{\mathrm{p}}\right)^{-1}\left(F_{ns}^{\mathrm{p}}\right)^{-1} \quad (A.12)$$

$$\frac{\partial \hat{D}_{ij}^{\mathrm{p}}}{\partial \hat{a}_{q}} = \frac{1}{\eta}\left[\frac{\partial \bar{\Sigma}}{\partial \hat{a}_{q}}\hat{N}_{ij}^{\mathrm{p}} + \bar{\Sigma}\frac{\partial \hat{N}_{ij}^{\mathrm{p}}}{\partial \hat{a}_{q}}\right] \quad (A.13)$$

$$\frac{\partial \hat{a}_{q}}{\partial F_{mn}^{\mathrm{p}}} = \frac{1}{\|\hat{a}\|}\left[\delta_{qm} - \frac{1}{\|\hat{a}\|^{2}}\hat{A}_{qm}\right]a_{n}^{0} \quad (A.14)$$

with

$$\frac{\partial \Sigma_{ij}}{\partial F_{mn}^{\mathrm{e}}} = \mathbb{I}_{kmin}\sigma_{kl}\left(F_{jl}^{\mathrm{e}}\right)^{-1} + F_{ki}^{\mathrm{e}}\frac{\partial \sigma_{kl}}{\partial F_{mn}^{\mathrm{e}}}\left(F_{jl}^{\mathrm{e}}\right)^{-1} - F_{ki}^{\mathrm{e}}\sigma_{kl}\left(F_{jm}^{\mathrm{e}}\right)^{-1}\left(F_{nl}^{\mathrm{e}}\right)^{-1} \quad (A.15)$$

$$\frac{\partial \hat{N}_{ij}^{p}}{\partial \Sigma_{kl}^{\mathrm{sym}}} = \frac{1}{\bar{\Sigma}}\left(\frac{\partial^{2}\hat{I}_{1}}{\partial \Sigma_{kl}^{\mathrm{sym}}\partial \Sigma_{ij}^{\mathrm{sym}}} + \alpha_{2}\frac{\partial^{2}\hat{I}_{2}}{\partial \Sigma_{kl}^{\mathrm{sym}}\partial \Sigma_{ij}^{\mathrm{sym}}} - \hat{N}_{kl}^{p}\hat{N}_{ij}^{p}\right) \quad (A.16)$$

$$\frac{\partial \bar{\Sigma}}{\partial \hat{a}_{m}} = \frac{1}{\bar{\Sigma}}\left(\frac{\partial \hat{I}_{1}}{\partial \hat{a}_{m}} + \alpha_{2}\frac{\partial \hat{I}_{2}}{\partial \hat{a}_{m}}\right) \quad (A.17)$$

$$\frac{\partial \hat{N}_{ij}^{p}}{\partial \hat{a}_{m}} = \frac{1}{\bar{\Sigma}}\left(\frac{\partial^{2}\hat{I}_{1}}{\partial \hat{a}_{m}\partial \Sigma_{ij}^{\mathrm{sym}}} + \alpha_{2}\frac{\partial^{2}\hat{I}_{2}}{\partial \hat{a}_{m}\partial \Sigma_{ij}^{\mathrm{sym}}} - \hat{N}_{ij}^{p}\frac{\partial \bar{\Sigma}}{\partial \hat{a}_{m}}\right) \quad (A.18)$$

The derivative of the Cauchy stress with respect to the elastic deformation in Eq. (A.15) is given as

$$\frac{\partial \sigma_{ij}}{\partial F_{kl}^{\mathrm{e}}} = \frac{\partial \sigma_{ij}^{\mathrm{iso}}}{\partial F_{kl}^{\mathrm{e}}} + \frac{\partial \sigma_{ij}^{\mathrm{trn}}}{\partial F_{kl}^{\mathrm{e}}} \quad (A.19)$$

$$\frac{\partial \sigma_{ij}^{\mathrm{iso}}}{\partial F_{kl}^{\mathrm{e}}} = \frac{\mu}{J^{\mathrm{e}}}\left(\frac{\partial B_{ij}^{\mathrm{e}}}{\partial F_{kl}^{\mathrm{e}}} - (B_{ij}^{\mathrm{e}} - \delta_{ij})(F_{kl}^{\mathrm{e}})^{-\mathrm{T}}\right) + \lambda J^{\mathrm{e}}\delta_{ij}(F_{kl}^{\mathrm{e}})^{-\mathrm{T}} \quad (A.20)$$

$$\frac{\partial \sigma_{ij}^{\mathrm{trn}}}{\partial F_{kl}^{\mathrm{e}}} = \frac{1}{J^{\mathrm{e}}}\left(\Phi_{ijkl}^{1} + \Phi_{ijkl}^{2} + \Phi_{ijkl}^{3}\right) - \frac{1}{J^{\mathrm{e}}}\sigma_{ij}^{\mathrm{trn}}(F_{kl}^{\mathrm{e}})^{-\mathrm{T}} \quad (A.21)$$

$$\Phi_{ijkl}^{1} = 2\beta(\xi_{2} - 1)\frac{\partial B_{ij}^{\mathrm{e}}}{\partial F_{kl}^{\mathrm{e}}} \quad (A.22)$$

$$\Phi_{ijkl}^{2} = 4\beta A_{ij}F_{kl}^{\mathrm{e}} \quad (A.23)$$

$$\Phi_{ijkl}^{3} = -\alpha\left(\frac{\partial B_{im}^{\mathrm{e}}}{\partial F_{kl}^{\mathrm{e}}}A_{mj} + \frac{\partial B_{jm}^{\mathrm{e}}}{\partial F_{kl}^{\mathrm{e}}}A_{im}\right) \quad (A.24)$$

$$\frac{\partial B_{ij}^{\mathrm{e}}}{\partial F_{kl}^{\mathrm{e}}} = F_{jl}^{\mathrm{e}}\delta_{ik} + F_{il}^{\mathrm{e}}\delta_{jk} \quad (A.25)$$

The other terms in Eq. (A.16)–(A.18) can be expanded as

$$\frac{\partial \hat{I}_1}{\partial \hat{a}_m} = \Sigma_{rs}^{\text{pind}} \frac{\partial \Sigma_{rs}^{\text{pind}}}{\partial \hat{a}_m} - \frac{\partial \hat{I}_2}{\partial \hat{a}_m} \tag{A.26}$$

$$\frac{\partial \hat{I}_2}{\partial \hat{a}_m} = \Sigma_{mj}^{\text{pind}} \Sigma_{jk}^{\text{pind}} \hat{a}_k + \hat{a}_q \Sigma_{qp}^{\text{pind}} \Sigma_{pm}^{\text{pind}} + \frac{\partial \hat{I}_2}{\partial \Sigma_{rs}^{\text{pind}}} \frac{\partial \Sigma_{rs}^{\text{pind}}}{\partial \hat{a}_m} \tag{A.27}$$

$$\frac{\partial^2 \hat{I}_1}{\partial \Sigma_{rs}^{\text{sym}} \partial \Sigma_{kl}^{\text{sym}}} = \left(\mathbb{P}_{ijrs} - \frac{\partial^2 \hat{I}_2}{\partial \Sigma_{rs}^{\text{sym}} \partial \Sigma_{ij}^{\text{pind}}} \right) \mathbb{P}_{ijkl} \tag{A.28}$$

$$\frac{\partial^2 \hat{I}_2}{\partial \Sigma_{rs}^{\text{sym}} \partial \Sigma_{kl}^{\text{sym}}} = \frac{\partial^2 \hat{I}_2}{\partial \Sigma_{rs}^{\text{sym}} \partial \Sigma_{ij}^{\text{pind}}} \mathbb{P}_{ijkl} \tag{A.29}$$

$$\frac{\partial^2 \hat{I}_1}{\partial \hat{a}_m \partial \Sigma_{kl}^{\text{sym}}} = \frac{\partial \hat{I}_1}{\partial \Sigma_{ij}^{\text{pind}}} \frac{\partial \mathbb{P}_{ijkl}}{\partial \hat{a}_m} + \left(\frac{\partial \Sigma_{ij}^{\text{pind}}}{\partial \hat{a}_m} - \frac{\partial^2 \hat{I}_2}{\partial \hat{a}_m \partial \Sigma_{ij}^{\text{pind}}} \right) \mathbb{P}_{ijkl} \tag{A.30}$$

$$\frac{\partial^2 \hat{I}_2}{\partial \hat{a}_m \partial \Sigma_{kl}^{\text{sym}}} = \frac{\partial \hat{I}_2}{\partial \Sigma_{ij}^{\text{pind}}} \frac{\partial \mathbb{P}_{ijkl}}{\partial \hat{a}_m} + \frac{\partial^2 \hat{I}_2}{\partial \hat{a}_m \partial \Sigma_{ij}^{\text{pind}}} \mathbb{P}_{ijkl} \tag{A.31}$$

where

$$\frac{\partial \Sigma_{rs}^{\text{pind}}}{\partial \hat{a}_m} = \frac{\partial \Sigma_{rs}^{\text{pind}}}{\partial \mathbb{P}_{ijkl}} \frac{\partial \mathbb{P}_{ijkl}}{\partial \hat{a}_m} \tag{A.32}$$

$$\frac{\partial \mathbb{P}_{ijkl}}{\partial \hat{a}_m} = \frac{\partial \mathbb{P}_{ijkl}}{\partial \hat{A}_{rs}} \frac{\partial \hat{A}_{rs}}{\partial \hat{a}_m} \tag{A.33}$$

$$\frac{\partial^2 \hat{I}_2}{\partial \hat{a}_m \partial \Sigma_{ij}^{\text{pind}}} = \left(\frac{\partial \hat{A}_{ir}}{\partial \hat{a}_m} \Sigma_{rj}^{\text{pind}} + \hat{A}_{ir} \frac{\partial \Sigma_{rj}^{\text{pind}}}{\partial \hat{a}_m} + \frac{\partial \Sigma_{ir}^{\text{pind}}}{\partial \hat{a}_m} \hat{A}_{rj} + \Sigma_{ir}^{\text{pind}} \frac{\partial \hat{A}_{rj}}{\partial \hat{a}_m} \right) \tag{A.34}$$

The remaining derivatives can be computed at each *internal* iteration

$$\frac{\partial^2 \hat{I}_2}{\partial \Sigma_{rs}^{\text{sym}} \partial \Sigma_{ij}^{\text{pind}}} = \left(\hat{A}_{im} \mathbb{P}_{mjrs} + \mathbb{P}_{imrs} \hat{A}_{mj} \right) \tag{A.35}$$

$$\frac{\partial \hat{I}_1}{\partial \Sigma_{rs}^{\text{pind}}} = 2 \Sigma_{rs}^{\text{pind}} \tag{A.36}$$

$$\frac{\partial \hat{I}_2}{\partial \Sigma_{rs}^{\text{pind}}} = \hat{A}_{rk} \Sigma_{ks}^{\text{pind}} + \Sigma_{rj}^{\text{pind}} \hat{A}_{js} \tag{A.37}$$

$$\frac{\partial \Sigma_{rs}^{\text{pind}}}{\partial \mathbb{P}_{ijkl}} = \delta_{ir} \delta_{js} \Sigma_{kl} \tag{A.38}$$

$$\frac{\partial \mathbb{P}_{ijkl}}{\partial \hat{A}_{rs}} = -\frac{3}{2} \left(\delta_{ir} \delta_{js} \hat{A}_{kl} + \hat{A}_{ij} \delta_{kr} \delta_{ls} \right) + \frac{1}{2} \left(\delta_{kl} \delta_{ir} \delta_{js} + \delta_{ij} \delta_{kr} \delta_{ls} \right) \tag{A.39}$$

$$\frac{\partial \hat{A}_{rs}}{\partial \hat{a}_m} = \delta_{rm} \hat{a}_s + \hat{a}_r \delta_{sm} \tag{A.40}$$

Appendix B. Derivatives external scheme

• The derivatives in Eq. (46) are given as

$$\frac{\partial R_{a_\sigma}}{\partial \bar{\sigma}} = -\frac{1}{\sigma_0} \left[\sinh^{-1}(\bar{\sigma}/\sigma_0) - \frac{\bar{\sigma}}{\sigma_0} \frac{\cosh(\bar{\sigma}/\sigma_0)}{\sinh^2(\bar{\sigma}/\sigma_0)} \right] \exp\left(-\mu \frac{I_3}{\sigma_0} \right) \tag{B.1}$$

$$\frac{\partial R_{a_\sigma}}{\partial I_3} = \frac{\bar{\sigma}/\sigma_0}{\sinh(\bar{\sigma}/\sigma_0)} \exp\left(-\mu \frac{I_3}{\sigma_0} \right) \frac{\mu}{\sigma_0} \tag{B.2}$$

$$\frac{\partial I_3}{\partial \sigma} = \left(\mathbf{I} - \bar{\mathbf{A}} \right) \tag{B.3}$$

• Applying the chain rule to the second term on the RHS of Eq. (51) yields

$$\frac{\partial \mathbf{R}_{\mathbf{F}_{pi}}}{\partial a_\sigma} = -\frac{\partial f_i}{\partial \Pi_i} : \frac{\partial \Pi_i}{\partial \hat{\mathbf{D}}_{pi}} : \frac{\partial \hat{\mathbf{D}}_{pi}}{\partial a_\sigma} \tag{B.4}$$

where $\partial \hat{\mathbf{D}}_{p,i} / \partial a_\sigma = -\bar{\sigma}/\left(\eta_{0i} a_\sigma^2\right) \hat{\mathbf{N}}_{p,i} = -1/a_\sigma \hat{\mathbf{D}}_{p,i}$ The expressions for $\partial f_i / \partial \Pi_i$ and $\partial \Pi_i / \partial \hat{\mathbf{D}}_{pi}$ are given by Eq. (A.5) and (A.6), respectively.

Appendix C. Derivatives for consistent tangent modulus

• The derivative $\partial \mathbf{R}_{\mathbf{F}_{pi}} / \partial \mathbf{F}$ in Eq. (55) reads

$$\frac{\partial \mathbf{R}_{\mathbf{F}_{pi}}}{\partial \mathbf{F}} = -\frac{\partial f}{\partial \Pi} : \frac{\partial \Pi}{\partial \hat{\mathbf{D}}_{pi}} : \frac{\partial \hat{\mathbf{D}}_{pi}}{\partial \Sigma_i^{\text{sym}}} : \frac{\partial \Sigma_i^{\text{sym}}}{\partial \Sigma_i} : \left[\frac{\partial \Sigma_i}{\partial \mathbf{F}_{ei}} : \frac{\partial \mathbf{F}_{ei}}{\partial \mathbf{F}} + \frac{\partial \Sigma_i}{\partial \sigma_i} : \frac{\partial \sigma_i}{\partial a} \cdot \frac{\partial a}{\partial \mathbf{F}} \right] \tag{C.1}$$

The derivatives $\partial f / \partial \Pi$, $\partial \Pi / \partial \hat{\mathbf{D}}_{pi}$, $\partial \Sigma_i / \partial \mathbf{F}_{ei}$ and $\partial \sigma_i / \partial a$, are given by Eq. (A.5), (A.6), (A.15) and (C.3), respectively. The other terms can be derived by differentiating Equations (3), (6) and (12). Applying the chain rule to $\partial \hat{\mathbf{D}}_{pi} / \partial \Sigma^{\text{sym}}$ gives

$$\frac{\partial \hat{\mathbf{D}}_{pi}}{\partial \Sigma^{\text{sym}}} = \frac{1}{\eta_i} \left[\hat{\mathbf{N}}_{pi} \otimes \frac{\partial \bar{\Sigma}_i}{\partial \Sigma_i^{\text{sym}}} + \bar{\Sigma}^i \frac{\partial \hat{\mathbf{N}}_{pi}}{\partial \Sigma_i^{\text{sym}}} \right] \tag{C.2}$$

where $\partial \bar{\Sigma}_i / \partial \Sigma_i^{\text{sym}} = \hat{\mathbf{N}}_{pi}$ and $\partial \hat{\mathbf{N}}_{pi} / \partial \Sigma_i^{\text{sym}}$ is given by Eq. (A.16). The derivative $\partial \sigma_i / \partial a$ in Eq. (C.1) reads

$$\frac{\partial \sigma_i}{\partial a} = \frac{1}{J_{ei}} \left[\Lambda_1 + \Lambda_2 + \Lambda_3 + \Lambda_4 \right] \tag{C.3}$$

$$\Lambda_1 = 4 \beta_i \left(\mathbf{B}_{ei} \otimes a \right) \tag{C.4}$$

$$\Lambda_2 = 2 \left[\alpha_i + \beta_i \left(\xi_{1i} - 3 \right) + 2\gamma \left(\xi_{2i} - 1 \right) \right] \frac{\partial \mathbf{A}}{\partial a} \tag{C.5}$$

$$\Lambda_3 = 8 \gamma_i \left(\mathbf{A} \otimes a \right) \tag{C.6}$$

$$\Lambda_4 = -\alpha_i \left(\mathbf{B}_{ei} \cdot \frac{\partial \mathbf{A}}{\partial a} + \frac{\partial \mathbf{A}}{\partial a} \cdot \mathbf{B}_{ei} \right) \tag{C.7}$$

where derivative $\partial \mathbf{A} / \partial a$ is given in Eq. (A.40), by replacing $\hat{\mathbf{A}}$ and $\hat{a}$ with $\mathbf{A}$ and a.

• The derivative $\partial R_{a_\sigma} / \partial \mathbf{F}$ in equation Eq. (57) reads

$$\frac{\partial R_{a_\sigma}}{\partial \mathbf{F}} = \left[\frac{\partial R_{a_\sigma}}{\partial \bar{\sigma}} \frac{\partial \bar{\sigma}}{\partial \sigma} + \frac{\partial R_\sigma}{\partial I_3} \frac{\partial I_3}{\partial \sigma} \right] : \sum_i^N \frac{\partial \sigma_i}{\partial \mathbf{F}} + \left[\frac{\partial R_\sigma}{\partial \bar{\sigma}} \frac{\partial \bar{\sigma}}{\partial \bar{a}} + \frac{\partial R_{a_\sigma}}{\partial I_3} \frac{\partial I_3}{\partial \bar{a}} \right] \cdot \frac{\partial \bar{a}}{\partial \mathbf{F}} \tag{C.8}$$

where the $\partial R_{a_\sigma} / \partial \bar{\sigma}$, $\partial R_{a_\sigma} / \partial I_3$, $\partial I_3 / \partial \sigma$ are given by Eq. (B.1)–(B.3), respectively. Derivative $\partial \bar{a} / \partial \mathbf{F}$ is given by Eq. (A.14), replacing $\hat{a}$ by a. The other derivatives read

$$\frac{\partial I_3}{\partial \bar{a}} = -2\sigma \cdot \bar{a} \tag{C.9}$$

$$\frac{\partial \bar{\sigma}}{\partial \bar{a}} = \frac{1}{\bar{\sigma}} \left(\frac{\partial I_1}{\partial \bar{a}} + \alpha_2 \frac{\partial I_2}{\partial \bar{a}} \right) \tag{C.10}$$

$$\frac{\partial \bar{\sigma}}{\partial \sigma} = \frac{1}{\bar{\sigma}} \left(\frac{\partial I_1}{\partial \sigma} + \alpha_2 \frac{\partial I_2}{\partial \sigma} \right) \tag{C.11}$$

$$\frac{\partial \sigma_i}{\partial \mathbf{F}} = \frac{\partial \sigma_i}{\partial \mathbf{F}_{ei}} : \left[\frac{\partial \mathbf{F}_{ei}}{\partial \mathbf{F}} + \frac{\partial \mathbf{F}_{ei}}{\partial \mathbf{F}_{pi}} : \frac{\partial \mathbf{F}_{pi}}{\partial \mathbf{F}} \right] + \frac{\partial \sigma_i}{\partial a} \cdot \frac{\partial a}{\partial \mathbf{F}} \tag{C.12}$$

where $\{\partial I_j / \partial \bar{a}\}_{j=1,2}$ and $\{\partial I_j / \partial \sigma\}_{j=1,2}$ are derived in Section 2.3.2 and can be found by replacing *intermediate* configuration quantities Σ_i^{pind} and $\hat{a}_i$ for each mode i by *total current* configuration quantities σ and a. The derivative $\partial \mathbf{F}_{pi} / \partial \mathbf{F}$ in Eq. (C.12) is found by solving the first consistency condition (see Eq. (55)).

Data availability

Data presented in this article are available at the 4TU.ResearchData repository through https://doi.org/10.4121/31233fa5-228f-448d-a415-e6a7b6f8e6b4.

References

Akkerman, R., Bouwman, M., Wijskamp, S., 2020. Analysis of the thermoplastic composite overmolding process: Interface Strength. Front. Mater. 7, 27. http://dx.doi.org/10.3389/fmats.2020.00027.

Amiri-Rad, A., Hütter, M., Govaert, L., Van Dommelen, J., 2021. Improved associated flow rule for anisotropic viscoplasticity in thermoplastic polymer systems. Mech. Mater. 163, 104087. http://dx.doi.org/10.1016/j.mechmat.2021.104087.

Amiri-Rad, A., Pastukhov, L., Govaert, L., Van Dommelen, J., 2019. An anisotropic viscoelastic-viscoplastic model for short-fiber composites. Mech. Mater. 137, 103141. http://dx.doi.org/10.1016/j.mechmat.2019.103141.

Baaser, H., 2004. The padé-approximation for matrix exponentials applied to an integration algorithm preserving plastic incompressibility. Comput. Mech. 34 (3), http://dx.doi.org/10.1007/s00466-004-0568-y.

Boehler, J.P. (Ed.), 1987. Applications of Tensor Functions in Solid Mechanics. Springer Vienna, Vienna, http://dx.doi.org/10.1007/978-3-7091-2810-7.

Bonet, J., Burton, A., 1998. A simple orthotropic, transversely isotropic hyperelastic constitutive equation for large strain computations. Comput. Methods Appl. Mech. Engrg. 162 (1–4), 151–164. http://dx.doi.org/10.1016/S0045-7825(97)00339-3.

Boyce, M.C., Montagut, E.L., Argon, A.S., 1992. The effects of thermomechanical coupling on the cold drawing process of glassy polymers. Polym. Eng. Sci. 32 (16), 1073–1085. http://dx.doi.org/10.1002/pen.760321605.

Boyce, M.C., Parks, D.M., Argon, A.S., 1988. Large inelastic deformation of glassy polymers. Part I: Rate dependent constitutive model. Mech. Mater. 7 (1), 15–33. http://dx.doi.org/10.1016/0167-6636(88)90003-8.

Boyce, M., Weber, G., Parks, D., 1989. On the kinematics of finite strain plasticity. J. Mech. Phys. Solids 37 (5), 647–665. http://dx.doi.org/10.1016/0022-5096(89)90033-1.

Brinson, H.F., Brinson, L.C., 2015. Polymer Engineering Science and Viscoelasticity: An Introduction. Springer US, Boston, MA, http://dx.doi.org/10.1007/978-1-4899-7485-3.

Dafalias, Y.F., 1998. Plastic spin: Necessity or redundancy? Int. J. Plast. 14 (9), 909–931. http://dx.doi.org/10.1016/S0749-6419(98)00036-9.

Daghia, F., Lagache, A., Di Gennaro, L., 2023. Validation of a new viscoelastic model for unidirectional polymer matrix composites by analytical and numerical homogenisation. Eur. J. Mech. A Solids 100, 104975. http://dx.doi.org/10.1016/j.euromechsol.2023.104975.

Dean, A., Sahraee, S., Reinoso, J., Rolfes, R., 2016. Finite deformation model for short fiber reinforced composites: Application to hybrid metal-composite clinching joints. Compos. Struct. 151, 162–171. http://dx.doi.org/10.1016/j.compstruct.2016.02.045.

Eidel, B., 2004. Anisotropic Inelasticity Modelling, Simulation, Validation (Ph.D. thesis). Technical University Darmstadt.

Erartsin, O., Amiri-Rad, A., Van Drongelen, M., Govaert, L.E., 2022. Time-dependent failure of off-axis loaded unidirectional glass/ iPP composites. J. Appl. Polym. Sci. 139 (23), 52293. http://dx.doi.org/10.1002/app.52293.

Eterovic, A.L., Bathe, K.-J., 1990. A hyperelastic-based large strain elasto-plastic constitutive formulation with combined isotropic-kinematic hardening using the logarithmic stress and strain measures. Internat. J. Numer. Methods Engrg. 30 (6), 1099–1114. http://dx.doi.org/10.1002/nme.1620300602.

Eyring, H., 1936. Viscosity, plasticity, and diffusion as examples of absolute reaction rates. J. Chem. Phys. 4 (4), 283–291. http://dx.doi.org/10.1063/1.1749836.

Gerbaud, P.-W., Otero, F., Bussetta, P., Camanho, P., 2019. An invariant based transversely-isotropic constitutive model for unidirectional fibre reinforced composites considering the matrix viscous effects. Mech. Mater. 138, 103146. http://dx.doi.org/10.1016/j.mechmat.2019.103146.

Govaert, L., Schellens, H., Thomassen, H., Smit, R., Terzoli, L., Peijs, T., 2001. A micromechanical approach to time-dependent failure in off-axis loaded polymer composites. Compos. Part A: Appl. Sci. Manuf. 32 (12), 1697–1711. http://dx.doi.org/10.1016/S1359-835X(01)00028-8.

Govaert, L.E., Timmermans, P.H.M., Brekelmans, W.A.M., 2000. The influence of intrinsic strain softening on strain localization in polycarbonate: Modeling and experimental validation. J. Eng. Mater. Technol. 122 (2), 177–185. http://dx.doi.org/10.1115/1.482784.

Haward, R.N., Thackray, G., 1968. The use of a mathematical model to describe isothermal stress-strain curves in glassy thermoplastics. Proc. R. Soc. Lond. Ser. A. Math. Phys. Sci. 302 (1471), 453–472. http://dx.doi.org/10.1098/rspa.1968.0029.

Hill, R., 1948. A theory of the yielding and plastic flow of anisotropic metals. Proc. R. Soc. Lond. Ser. A. Math. Phys. Sci. 193 (1033), 281–297. http://dx.doi.org/10.1098/rspa.1948.0045.

Hofman, P., Van Der Meer, F., Sluys, L., 2024. A numerical framework for simulating progressive failure in composite laminates under high-cycle fatigue loading. Eng. Fract. Mech. 295, 109786. http://dx.doi.org/10.1016/j.engfracmech.2023.109786.

Ke, L., Van Der Meer, F., 2022. A computational homogenization framework with enhanced localization criterion for macroscopic cohesive failure in heterogeneous materials. J. Theor. Comput. Appl. Mech. 7707. http://dx.doi.org/10.46298/jtcam.7707.

Khaleghi, H., Amiri-Rad, A., Mashayekhi, M., 2022. A thermodynamically consistent continuum damage model for time-dependent failure of thermoplastic polymers. Int. J. Plast. 154, 103278. http://dx.doi.org/10.1016/j.ijplas.2022.103278.

Klompen, E.T.J., Engels, T.A.P., Govaert, L.E., Meijer, H.E.H., 2005. Modeling of the postyield response of glassy polymers: Influence of thermomechanical history. Macromolecules 38 (16), 6997–7008. http://dx.doi.org/10.1021/ma050498v.

Klompen, E.T.J., Govaert, L.E., 1999. Nonlinear viscoelastic behaviour of thermorheologically complex materials. Mech. Time-Dependent Mater. 3, 49–69.

Koerber, H., Kuhn, P., Ploeckl, M., Otero, F., Gerbaud, P.-W., Rolfes, R., Camanho, P.P., 2018. Experimental characterization and constitutive modeling of the non-linear stress–strain behavior of unidirectional carbon–epoxy under high strain rate loading. Adv. Model. Simul. Eng. Sci. 5 (1), 17. http://dx.doi.org/10.1186/s40323-018-0111-x.

Kovačević, D., Sundararajan, B.K., van der Meer, F.P., 2022. Microscale modeling of rate-dependent failure in thermoplastic composites under off-axis loading. Eng. Fract. Mech. preprint, http://dx.doi.org/10.1016/j.engfracmech.2022.108884.

Kovačević, D., Sundararajan, B.K., Van Der Meer, F.P., 2024. Micromechanical model for off-axis creep rupture in unidirectional composites undergoing finite strains. Compos. Part A: Appl. Sci. Manuf. 176, 107860. http://dx.doi.org/10.1016/j.compositesa.2023.107860.

Kovačević, D., van der Meer, F.P., 2022. Strain-rate based arclength model for nonlinear microscale analysis of unidirectional composites under off-axis loading. Int. J. Solids Struct. 250 (December 2021), 111697. http://dx.doi.org/10.1016/j.ijsolstr.2022.111697.

Kröner, E., 1959. Allgemeine kontinuumstheorie der versetzungen und eigenspannungen. Arch. Ration. Mech. Anal. 4 (1), 273–334. http://dx.doi.org/10.1007/BF00281393.

Larsson, R., Singh, V., Olsson, R., Marklund, E., 2020. A micromechanically based model for strain rate effects in unidirectional composites. Mech. Mater. 148, 103491. http://dx.doi.org/10.1016/j.mechmat.2020.103491.

Lee, E.H., 1969. Elastic-plastic deformation at finite strains. ASMEJ. Appl. Mech. March 36 (1), 1–6.

Lenders, T., Remmers, J.J.C., Pini, T., Veenstra, P., Govaert, L.E., Geers, M.G.D., 2023. An elasto-viscoplastic constitutive model for the rate-dependent behavior of polyvinylidene fluoride. J. Polym. Sci. 61 (14), 1439–1456. http://dx.doi.org/10.1002/pol.20220729.

Lenders, T., Remmers, J.J., Pini, T., Veenstra, P., Govaert, L.E., Geers, M.G., 2024. A periodic micromechanical model for the rate- and temperature-dependent behavior of unidirectional carbon fiber-reinforced PVDF. J. Reinf. Plast. Compos. 07316844241266012. http://dx.doi.org/10.1177/07316844241266012.

Liu, Y., Van Der Meer, F., Sluys, L., Fan, J., 2020. A numerical homogenization scheme used for derivation of a homogenized viscoelastic-viscoplastic model for the transverse response of fiber-reinforced polymer composites. Compos. Struct. 252, 112690. http://dx.doi.org/10.1016/j.compstruct.2020.112690.

Lubliner, J., 2008. Plasticity Theory. Courier Corporation.

Maia, M., Rocha, I., Kerfriden, P., Van Der Meer, F., 2023. Physically recurrent neural networks for path-dependent heterogeneous materials: Embedding constitutive models in a data-driven surrogate. Comput. Methods Appl. Mech. Engrg. 407, 115934. http://dx.doi.org/10.1016/j.cma.2023.115934.

Maia, M.A., Rocha, I.B.C.M., Kovačević, D., van der Meer, F.P., 2025. Surrogate-based multiscale analysis of experiments on thermoplastic composites under off-axis loading. http://dx.doi.org/10.48550/arXiv.2501.10193, arXiv:2501.10193.

Mandel, J., 1972. Plasticite Classique et Viscoplasticite. In: CISM International Centre for Mechanical Sciences, Springer.

Neveu, F., Cornu, C., Olivier, P., Castanié, B., 2022. Manufacturing and impact behaviour of aeronautic overmolded grid-stiffened thermoplastic carbon plates. Compos. Struct. 284, 115228. http://dx.doi.org/10.1016/j.compstruct.2022.115228.

Oliver, J., Caicedo, M., Roubin, E., Huespe, A., Hernández, J., 2015. Continuum approach to computational multiscale modeling of propagating fracture. Comput. Methods Appl. Mech. Engrg. 294, 384–427. http://dx.doi.org/10.1016/j.cma.2015.05.012.

Rodrigues Lopes, I.A., Camanho, P.P., Andrade Pires, F.M., Arteiro, A., 2022. An invariant-based elasto-visco-plastic model for unidirectional polymer composites at finite strains. Int. J. Solids Struct. 236–237, 111292. http://dx.doi.org/10.1016/j.ijsolstr.2021.111292.

Sansour, C., Kollmann, F.G., 1998. Large viscoplastic deformations of shells. Theory and finite element formulation. Comput. Mech. 21 (6), 512–525. http://dx.doi.org/10.1007/s004660050329.

Senden, D., Peters, G., Govaert, L., Van Dommelen, J., 2013. Anisotropic yielding of injection molded polyethylene: Experiments and modeling. Polymer 54 (21), 5899–5908. http://dx.doi.org/10.1016/j.polymer.2013.08.047.

Singh, V., Larsson, R., Olsson, R., Marklund, E., 2023. A micromechanics based model for rate dependent compression loaded unidirectional composites. Compos. Sci. Technol. 232, 109821. http://dx.doi.org/10.1016/j.compscitech.2022.109821.

Spencer, A., 1972. Deformations of Fibre-Reinforced Materials. In: Oxford Science Research Papers, Clarendon Press.

Spencer, A.J.M., 1987. Kinematic constraints, constitutive equations and failure rules for anisotropic materials. In: Boehler, J.P. (Ed.), Applications of Tensor Functions in Solid Mechanics. Springer, Vienna, pp. 187–201. http://dx.doi.org/10.1007/978-3-7091-2810-7_10.

Sun, C., Chung, I., 1993. An oblique end-tab design for testing off-axis composite specimens. Composites 24 (8), 619–623. http://dx.doi.org/10.1016/0010-4361(93)90124-Q.

Sundararajan, B.K., 2024. Matrix Dominated Failure in Continuous Carbon Fibre Reinforced Poly(Ether Ether Ketone) (Ph.D. thesis). University of Twente, Enschede, The Netherlands, http://dx.doi.org/10.3990/1.9789036560405.

Tervoort, T.A., Klompen, E.T.J., Govaert, L.E., 1996. A multi-mode approach to finite, three-dimensional, nonlinear viscoelastic behavior of polymer glasses. J. Rheol. 40 (5), 779–797. http://dx.doi.org/10.1122/1.550755.

Tervoort, T.A., Smit, R.J.M., Brekelmans, W.A.M., Govaert, L.E., 1998. A constitutive equation for the elasto-viscoplastic deformation of glassy polymers. Mech. Time-Dependent Mater. 1: 269–291, 1998 1, 269–291. http://dx.doi.org/10.1023/A:1009720708029.

Timmis, A.J., Hodzic, A., Koh, L., Bonner, M., Soutis, C., Schäfer, A.W., Dray, L., 2015. Environmental impact assessment of aviation emission reduction through the implementation of composite materials. Int. J. Life Cycle Assess. 20 (2), 233–243. http://dx.doi.org/10.1007/s11367-014-0824-0.

Valverde, M.A., Kupfer, R., Kawashita, L.F., Gude, M., Hallett, S.R., 2018. Effect of processing parameters on quality and strength in thermoplastic composite injection overmoulded components. In: 18th European Conference on Composite Materials. Applied Mechanics Laboratory.

Valverde, M., Kupfer, R., Wollmann, T., Kawashita, L., Gude, M., Hallett, S., 2020. Influence of component design on features and properties in thermoplastic over-moulded composites. Compos. Part A: Appl. Sci. Manuf. 132, 105823. http://dx.doi.org/10.1016/j.compositesa.2020.105823.

Van Breemen, L., Klompen, E., Govaert, L., Meijer, H., 2011. Extending the EGP constitutive model for polymer glasses to multiple relaxation times. J. Mech. Phys. Solids 59 (10), 2191–2207. http://dx.doi.org/10.1016/j.jmps.2011.05.001.

Van Der Meer, F.P., 2016. Micromechanical validation of a mesomodel for plasticity in composites. Eur. J. Mech. A Solids 60, 58–69. http://dx.doi.org/10.1016/j.euromechsol.2016.06.008.

Van Erp, T.B., Reynolds, C.T., Peijs, T., Van Dommelen, J.A.W., Govaert, L.E., 2009. Prediction of yield and long-term failure of oriented polypropylene: Kinetics and anisotropy. J. Polym. Sci. Part B: Polym. Phys. 47 (20), 2026–2035. http://dx.doi.org/10.1002/polb.21801.

Vogler, M., Rolfes, R., Camanho, P., 2013. Modeling the inelastic deformation and fracture of polymer composites – Part I: Plasticity model. Mech. Mater. 59, 50–64. http://dx.doi.org/10.1016/j.mechmat.2012.12.002.

Weber, G., Anand, L., 1990. Finite deformation constitutive equations and a time integration procedure for isotropic, hyperelastic-viscoplastic solids. Comput. Methods Appl. Mech. Engrg. 79 (2), 173–202. http://dx.doi.org/10.1016/0045-7825(90)90131-5.